Miner Deposita
DOI 10.1007/s00126-016-0684-6

ARTICLE

# Mineralisation footprints and regional timing of the world-class Siguiri orogenic gold district (Guinea, West Africa)

**Erwann Lebrun[1] · Nicolas Thébaud[1] · John Miller[1] · Malcolm Roberts[2] · Noreen Evans[3]**

Received: 9 September 2015 / Accepted: 14 September 2016


**Abstract** Siguiri is a world-class orogenic gold district hosted in the weakly metamorphosed Upper Birimian to Lower Tarkwa Group sedimentary rocks of the Siguiri Basin (Guinea). The district is characterised by a protracted deformation history associated with four main deformation events: $D_{1S}$ is a N-S compression; $D_{2S}$ is an E-W compression progressively evolving into an early-$D_{3S}$ transpression and then into a late-$D_{3S}$ NNW-SSE transtension and $D_{4S}$ is a NE-SW compression. Field observations, petrography and geochemistry at three key deposits of the Siguiri district (Bidini, Sintroko PB1 and Kosise) suggest a polyphase hydrothermal history that can be subdivided into four hydrothermal events. The first hydrothermal event was associated with the development of barren bedding-parallel and en-echelon $V_{2S}$ quartz-dominated-(pyrite) veins. The second hydrothermal event is characterised by the development of $V_{3A}$ pyrite-ankerite veins late during $D_{3S}$. Laser ablation-ICP-MS data show that this vein set contains high gold contents of up to 43.3 ppm, in substitution in pyrite crystal lattice, representing a minor first gold mineralisation event. The third and most prominently developed hydrothermal event is late $D_{3S}$ and represents the second and principal gold mineralisation event. This mineralisation event led to two distinct mineralisation textures. The first texture is best exposed in the Kosise deposit and is characterised by gold-bearing quartz-ankerite-arsenopyrite conjugate $V_{3B}$ veins. Although the bulk of the gold is hosted in native gold grains in $V_{3B}$ veins, LA-ICP-MS analyses show that gold also substitutes in the arsenopyrite crystal lattice (up to 55.5 ppm). The second mineralisation texture is best expressed in the Sanu Tinti deposit and consists of disseminated barren pyrite hosted in a polymict conglomerate. The second and third hydrothermal events are both structurally controlled by a series of early-$D_{3S}$ N-S, NE-SW, WNW-ESE and E-W sub-vertical incipient structures expressed as fracture zones of higher $V_{3S}$ vein density. A composite geochemical cross section across fracture zones from the Kosise deposit indicates that gold mineralisation in the Siguiri district is associated with enrichments in Ag, Au, As, Bi, Co, Mo, (Sb), S, Te and W relative to background. Geochemical variations associated with the ore shoots in the Siguiri district are consistent with petrographic observations and highlight an albite-carbonate-sulphide-sericite alteration. The fourth and last hydrothermal event is associated with the development of a late penetrative $S_{4S}$ cleavage during $D_{4S}$ deformation, which overprints all pre-existing hydrothermal features and is associated with the deposition of free gold, chalcopyrite and galena along fractures in $V_{3A}$ pyrite and $V_{3B}$ pyrite and arsenopyrite. Mineralogical and geochemical footprints as well as timing of the gold-mineralising events in the Siguiri district, when compared with other deposits of the West African Craton, highlight the synchronicity of gold mineralisation in Siguiri (syn-$D_{3S}$ and syn-$D_{4S}$ events) with

Editorial handling: H. Frimmel

**Electronic supplementary material** The online version of this article (doi:10.1007/s00126-016-0684-6) contains supplementary material, which is available to authorized users.

✉ Erwann Lebrun
erwann.lebrun@gmail.com

[1] Centre for Exploration Targeting and ARC Centre of Excellence for Core to Crust Fluid Systems, School of Earth and Environment, The University of Western Australia, Robert Street Building, M006, 35 Stirling Highway, Crawley, WA 6009, Australia

[2] Centre for Microscopy, Characterisation and Analysis, The University of Western Australia, M010, 35 Stirling Highway, Crawley, WA 6009, Australia

[3] John de Laeter Centre for Isotope Research, TIGeR, Department of Applied Geology, Curtin University, Perth, WA 6845, Australia

Published online: 01 October 2016

other similar events in this part of the craton, such as the early Au-Sb-Bi-(Te-W) mineralisation at the Morila deposit in Southeast Mali. Our results support the hypothesis that late Eburnean-age gold mineralisation in the Siguiri district and in the West African Craton as a whole was polyphase.

**Keywords** West Africa · Siguiri · Orogenic gold · Laser ablation · Geochemistry · Timing · Polyphase · Targeting

## Introduction

Orogenic gold deposits typically encompass a wide variety of host rocks, metamorphic facies, mineral assemblages and textures, with variations in some cases observed within a single deposit (Groves et al. 2003; Goldfarb et al. 2005; Robert et al. 2005). Finding the footprint of orogenic gold mineralisation therefore represents a great challenge for exploration geologists (e.g. Groves et al. 2000; Neumayr et al. 2008). However, as the geochemical and petrological footprints of orogenic gold deposits are more extensive than the ore zone itself (Kishida and Kerrich 1987; Eilu and Mikucki 1998), characterisation of mineral alteration assemblages at the deposit scale provides the exploration geologist with useful vectoring tools for targeting (Eilu et al. 1999; Eilu and Groves 2001). Studies on the characterisation and quantification of trace elements in sulphides associated with orogenic gold deposits (Pitcairn et al. 2006; Large et al. 2011; Large et al. 2012) typically attempt to resolve the controversial source of mineralising fluids (Groves et al. 2003; Large et al. 2011; Tomkins 2013). However, trace element signatures of sulphides can also be used to distinguish between different sulphide generations attesting of a complex polyphase hydrothermal history (Zhao et al. 2011).

The wide diversity of gold mineralisation types recorded in the West African Craton, such as intrusion-related gold (McFarlane et al. 2011), orogenic gold (Oberthür et al. 1998; Allibone et al. 2002; Lawrence et al. 2013a; Fougerouse et al. 2016), palaeoplacers (Davis et al. 1994; Hirdes and Nunoo 1994) and porphyry Cu-Au deposits (Béziat et al. 2013), renders essential the detailed petrographic and geochemical characterisation of a deposit to resolve its nature and footprint. In turn, this footprint can become a backbone for exploration strategies.

This study focuses on characterisation of the mineral assemblages and mineralisation in three key deposits of the world-class orogenic gold Siguiri district (Guinea, West Africa) and its geochemical and petrological footprints. Siguiri is the only large (> 50 t Au) orogenic gold district currently known in the Siguiri Basin, one of the largest sedimentary basins of the West African Craton. Laser ablation-ICP-MS data are used to distinguish and in turn help constrain the relative timing of the different generations of pyrite, allowing the creation of a district-scale paragenetic sequence, which serves to highlight the polyphase nature of gold mineralisation in the Siguiri district. Comparison between the timing of the main gold mineralisation event in the district with events from other orogenic gold systems of the West African Craton can elucidate the temporal patterns of mineralisation on the regional scale.

## Geological context

The Siguiri district is located in the northwestern part of the Baoulé-Mossi domain, in the West African Craton (Lebrun et al. 2015a; Lebrun et al. 2015b). The district is in the Paleoproterozoic sedimentary basin of Siguiri, Guinea (Fig. 1). Mineralisation is hosted by three sedimentary formations (Fig. 2), all metamorphosed to sub-greenschist facies. To the east, the Balato Formation is dominated by fine-grained pelitic sedimentary rocks, such as shale and siltstone. It is overlain by the Fatoya Formation, which spreads in the centre of the district and is dominated by coarser sedimentary rocks, mainly greywacke and sandstone beds. The Kintinian Formation, to the west, overlies the Fatoya Formation and is characterised by shale with abundant centimetric interbeds of limestone and at least two decametric to hectometric interbeds of conglomerate. The three formations have been dated by U-Pb SHRIMP II on zircons at ca. 2115 Ma (Upper Birimian), and the Kintinian Formation is interpreted to be part of the Lower Tarkwa Group (Lebrun et al. 2015b).

Four deformation events have been recognised in the Siguiri district (Lebrun et al. 2015a). The first event, $D_{1S}$, is characterised by E-W folds and a discreet shallow dipping axial planar $S_{1S}$ cleavage. It was interpreted as the product of N-S compression. The second event, $D_{2S}$, was responsible for the bulk of the deformation and for the structural grain observed in the Siguiri Basin. The $F_{2S}$ folds crenulate $F_{1S}$ folds at a district scale and develop type 1 fold interference patterns (Ramsay and Huber 1987) at a deposit scale. The $D_{2S}$ event is associated with W-verging folds, the axial plane of which varies from NNE-SSW to NNW-SSE in strike. The plunge of the $F_{2S}$ fold axes varies from sub-vertical in the Balato Formation to almost sub-horizontal in the Fatoya Formation. No axial planar $S_{2S}$ cleavage was found to be associated with this event, which was interpreted to be due to a possible later overprint and erasure by the penetrative $S_{4S}$ fabric (Lebrun et al. 2015a). This second deformation event was interpreted as having been associated with an E-W to ENE-WSW compression associated with N-S thrust faults and E-W normal faults. This

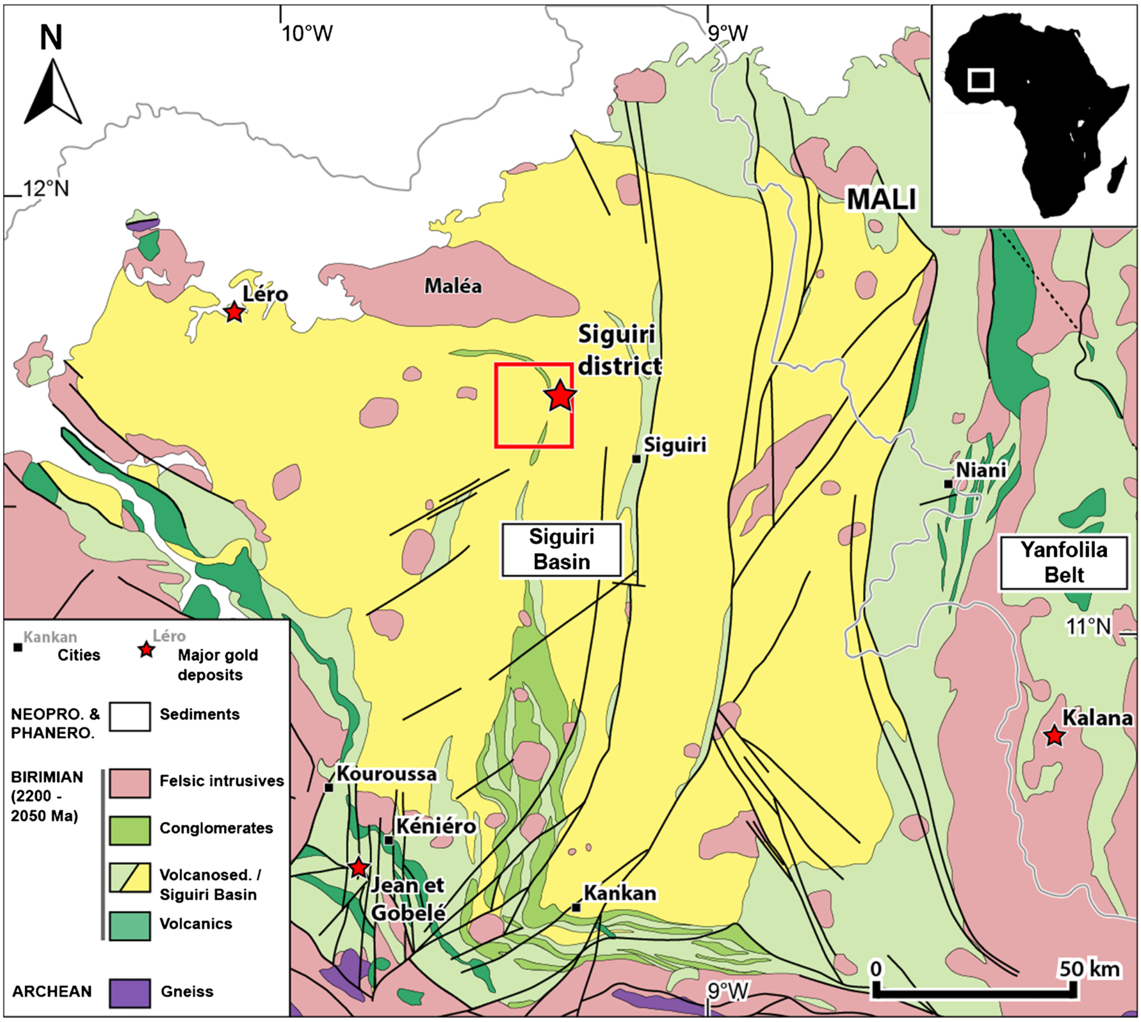


**Fig. 1** Geological map of the Siguiri Basin. Location of the Siguiri district map (Fig. 2) in *red*. After Milési et al. (1989), Miller et al. (2013) and Lebrun et al. (2015b)

deformation event progressively evolved to an early-$D_{3S}$ transpression, characterised by the reactivation of the N-S and E-W faults, and the development of NE-SW dextral and WNW-ESE sinistral shear zones (Fig. 2). In the Siguiri district, these structures are typically expressed as sub-vertical incipient structures, represented by discreet fracture zones associated with a 10- to 15-m-wide halo of increased vein density, developed during the late-$D_{3S}$ NNW-SSE transtensional event (Lebrun et al. 2015a). All structural elements in the Siguiri district were overprinted during the youngest deformation event, $D_{4S}$, which is characterised by local open $F_{4S}$ folds with sub-horizontal NE-SW-trending fold axes, affecting late-$D_{3S}$ structures. The $D_{4S}$ event is associated with a penetrative sub-vertical NNE-SSW $S_{4S}$ cleavage, axial planar to the $F_{4S}$ folds at the outcrop scale. This last deformation event was interpreted as having been associated with NW-SE compression (Lebrun et al. 2015a). The $S_{4S}$ cleavage parallels the supra-solidus magmatic fabric observed in the pre- to syn-tectonic Maléa monzogranite, which intrudes the Siguiri Basin fill to the north of the district (Fig. 1; Lebrun et al. 2015b).

Hydrothermal activity in the Siguiri district is mainly characterised by veining developed during $D_{2S}$ E-W compression and late-$D_{3S}$ NNW-SSE transtension. Syn-$D_{2S}$ veining is expressed as bedding parallel and en-echelon $V_{2S}$ vein arrays (Fig. 3) interpreted to have developed by flexural slip along bedding during $F_{2S}$ folding (Lebrun et al. 2015a). The $V_{2S}$ veins are cut by the $V_{3S}$ veins developed late during $D_{3S}$ transtension along the early-$D_{3S}$ faults. Based on drill core observations, two different vein sets were identified: $V_{3A}$ and $V_{3B}$ (Fig. 3). The $V_{3A}$ vein set commonly has brecciated structures and varies significantly in orientation across the district (Fig. 3c). The second vein set, $V_{3B}$, cuts both $V_{2S}$ and $V_{3A}$ sets but is overprinted by $S_{4S}$. The $V_{3B}$ vein set displays conjugate geometry, with individual veins dipping steeply or moderately to the SE. This vein set hosts the bulk of the gold mined in the Siguiri district.

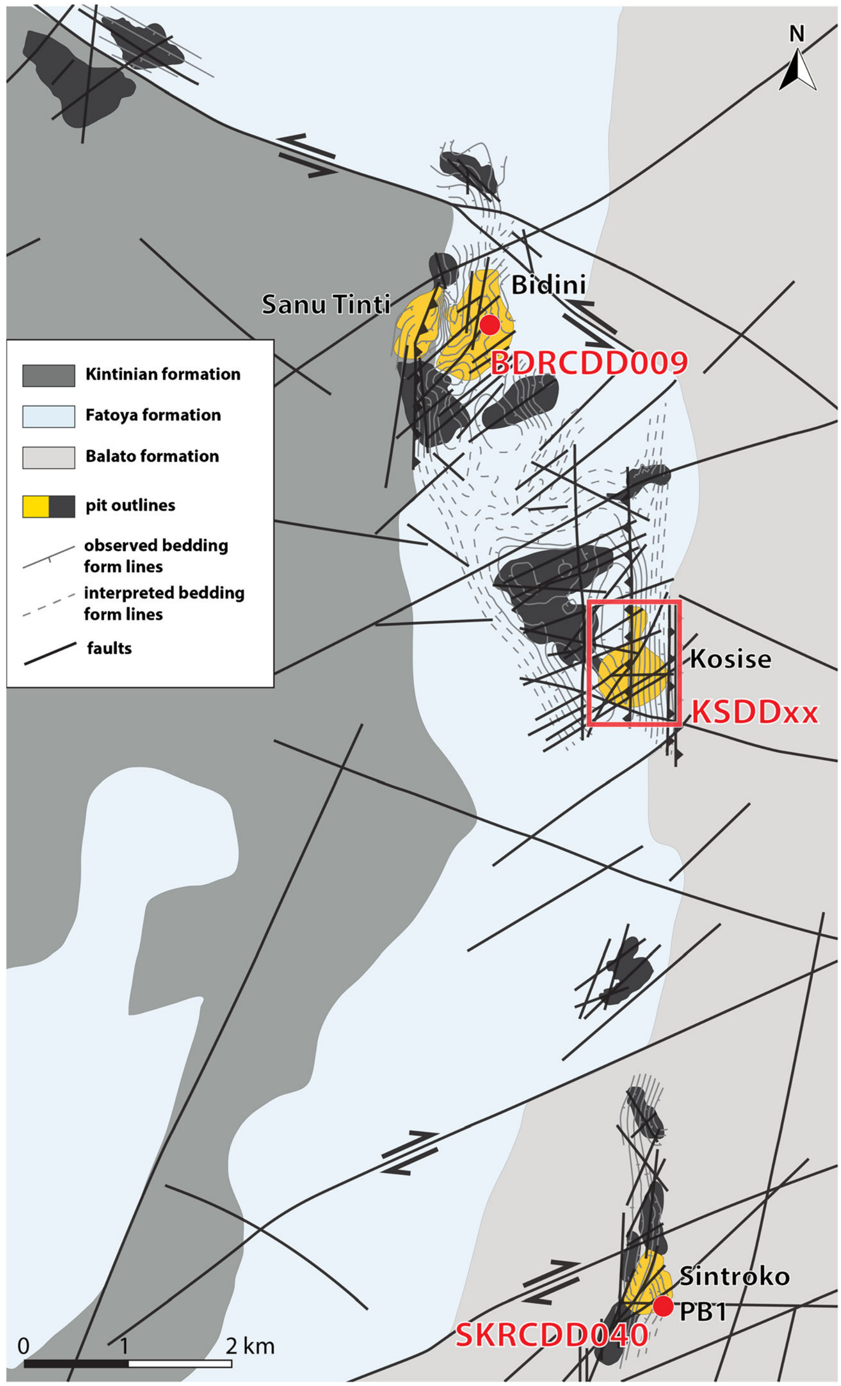


**Fig. 2** Map of the Siguiri gold district and its gold deposits showing bedding form lines. Locations of the logged drill holes and areas of interest highlighted in *red*. After Lebrun et al. (2015a)

## Methodology

### Field approach and sampling

Structural elements and controls on gold mineralisation in the Siguiri district are very consistent from one deposit to the next (Lebrun et al. 2015a). Three deposits were identified as representative of the Siguiri district mineralisation: the Bidini, Kosise and Sintroko PB1 deposits (Fig. 2). Extended field approach, sampling methodology and data tables can be found in the Electronic Supplementary Materials (or ESM; ESM 1 to 6).

Sampling was designed to (1) constrain the paragenesis of the district, (2) characterise the geochemical halo associated with a representative mineralised shear zone, (3) compare the geochemical changes between formations and host rocks and (4) compare the sulphide major and trace element concentrations and gold content of each vein generation and hydrothermal events. A total of 37 representative unaltered rock samples were collected from Bidini, Kosise and Sintroko PB1

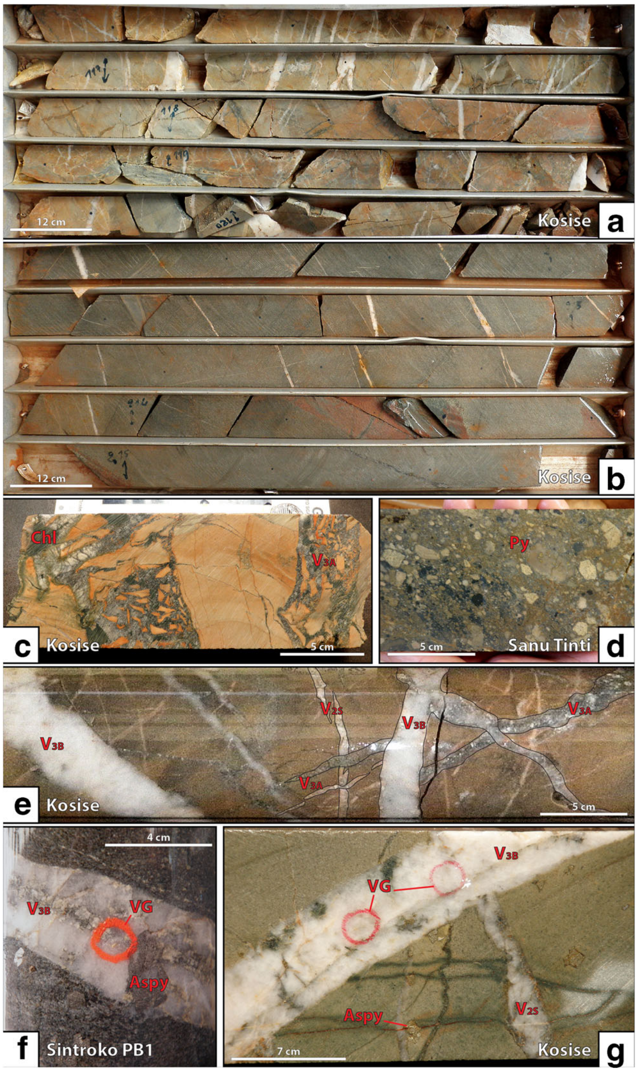


**Fig. 3** Photographs of **a** veining and alteration associated with a high-grade zone in the Kosise deposit (hole KSDD024); **b** example of an unaltered and unmineralised zone from the Kosise deposit (hole KSDD024, sample O); **c** example of $V_{3A}$ carbonate-pyrite breccia veins. Minor pyrite is accompanied by abundant chlorite; **d** Sanu Tinti style of mineralisation showing disseminated pyrite in a conglomerate interbed (hole BDRCDD009); **e** drill core from Kosise showing the crosscutting relationship between $V_{2S}$, $V_{3A}$ and $V_{3B}$ vein sets; **f** native gold found in the centre of an antitaxial $V_{3B}$ quartz-ankerite-arsenopyrite vein; **g** native gold in an antitaxial $V_{3B}$ quartz-ankerite-arsenopyrite vein overprinting a $V_{2S}$ quartz-(carbonate) vein. Chlorite is partially replacing the Fe-carbonates. *VG* visible gold

deposits as well as the Kami deposit, hosted in some of the same sedimentary beds as the Kosise deposit (ESM 1 and ESM 2 Table 1).

In order to characterise the geochemical variations associated with early-$D_{3S}$ mineralised faults, samples were collected along a NW-SE composite section, across a discrete NE-SW dextral shear zone in the Kosise deposit and across a NE-SW shear zone and a bedding-parallel N-S reverse fault (Fig. 4(C, D)). The Kosise deposit was chosen because it is hosted in the Fatoya Formation, host to most of the deposits (Fig. 2), and because its structural framework is relatively simple and well constrained. Veins were trimmed off from all samples to avoid “nugget effects” on gold geochemistry. The veins were retained and used to make polished thin sections, for subsequent LA-ICP-MS analyses on their associated sulphides (Table 1).

## Analytical work and data processing

### *Petrography and mineral chemistry*

Optical microscopy, electron microscopy and semi-quantitative analyses were conducted at the Centre for Exploration Targeting (CET) and Centre for Microscopy, Characterisation and Analysis (CMCA) at the University of Western Australia (UWA). Electron probe micro-analysis (EPMA) conducted at CMCA was used to determine the Fe and As content in the different generations of sulphides. Iron concentrations were later used as internal standards for laser ablation data processing. X-ray diffraction (XRD) conducted at CMCA was used to characterise the modal composition and its variations of the geochemical samples collected in the Kosise deposit. LA-ICP-MS was conducted at Curtin University and was used to measure and compare the composition of the different hydrothermal mineral assemblages observed in the Siguiri district. Extended petrography and mineral chemistry methodology can be found in ESM 1, ESM 2 Table 1, ESM 3 Table 2 and Table 2.

### *Whole-rock major and trace element geochemical analyses*

Whole-rock major and trace element compositions were measured on each sample in order to identify the geochemical variations associated with mineralisation in the three sedimentary formations hosting the Siguiri district, and the main geochemical differences between these formations (ESM 2 Table 1 and ESM 4 Table 3).

Geochemical backgrounds for the Balato, Fatoya and Kintinian formations were calculated following the cumulative frequency method proposed by Landry (1995), which follows the work conducted by Sinclair (1974, 1991) (ESM 5 Table 4). In addition, anomalous geochemical variations across the Kosise deposit geochemical transect were constrained by mass balance calculations following the work by Gresens (1967) and MacLean and Barrett (1993) updated by Grant (2005) and further refined by Mukherjee and Gupta (2008) and by López-Moro (2012) in his EASYGRESGRANT method (ESM 6 Table 5). Least-altered samples (ESM 1, ESM 2 Table 1), used for the calculations, were selected based on their distance from mineralised shear zones, visible signs of

**Table 1** Sample selection methodology used for the LA-ICP-MS analyses

| Mineral generation | V2A | V2B | V2C | D3S |
|---|---|---|---|---|
| Pyrite | Sampled from greywacke and shale beds in the Fatoya F. | Sampled from greywacke beds in the Fatoya F. | Sampled from greywacke beds in the Fatoya F. and conglomerate beds in the Kintinian F. | Sampled from greywacke beds in the Fatoya F. |
| Arsenopyrite | – | – | Sampled from greywacke beds in the Balato and Fatoya F. | – |

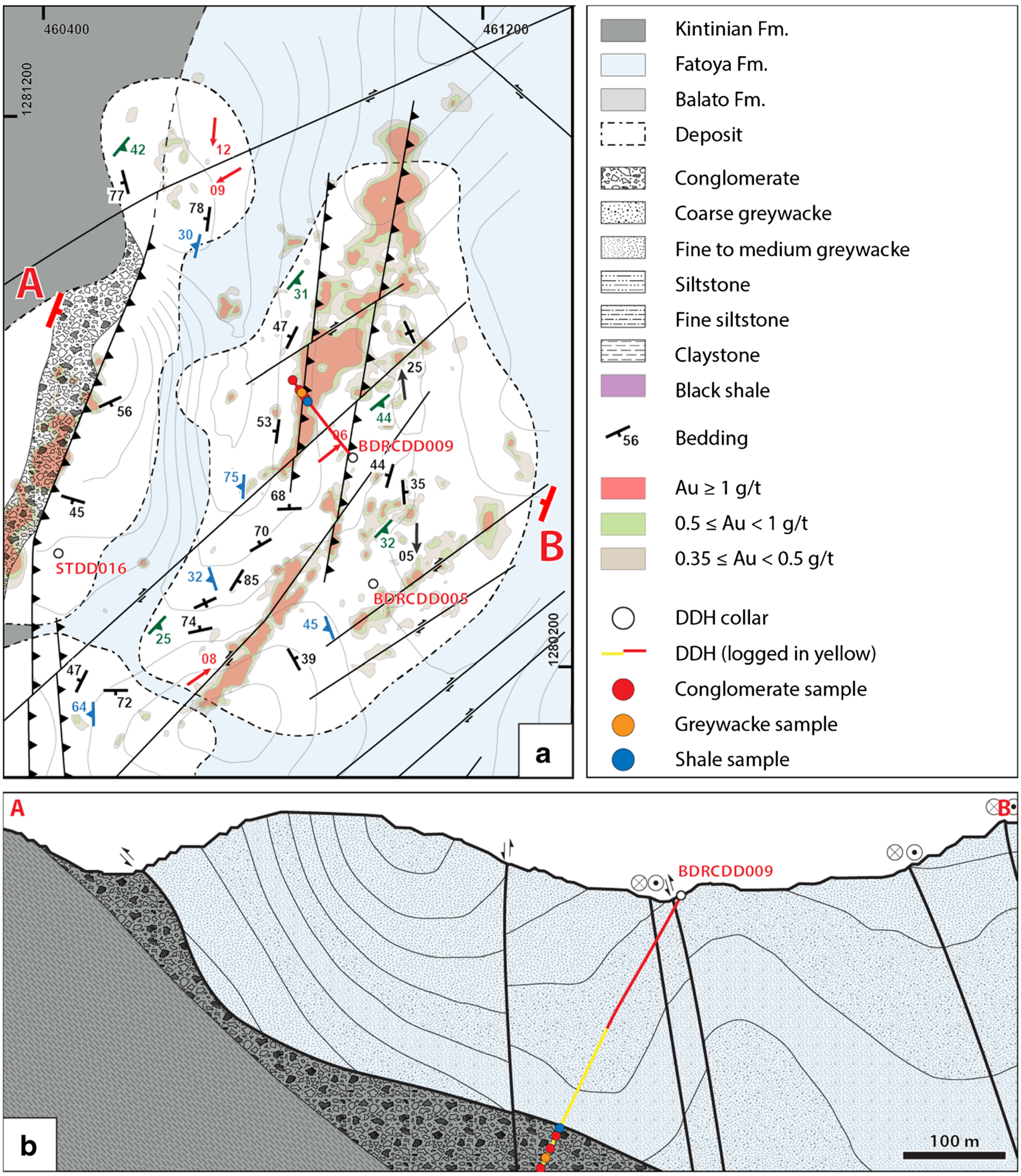


**Fig. 4** Simplified structural maps and cross sections of key deposits from the Siguiri district (location map on Fig. 2). *A* Structural map of Sanu Tinti and Bidini and *B* their cross section; *C* structural map and *D* cross section of Kosise; *E* structural map and *F* cross section of Sintroko PB1. Locations of the drill holes and collected samples *highlighted*. Orthonormal scale (no vertical exaggeration)

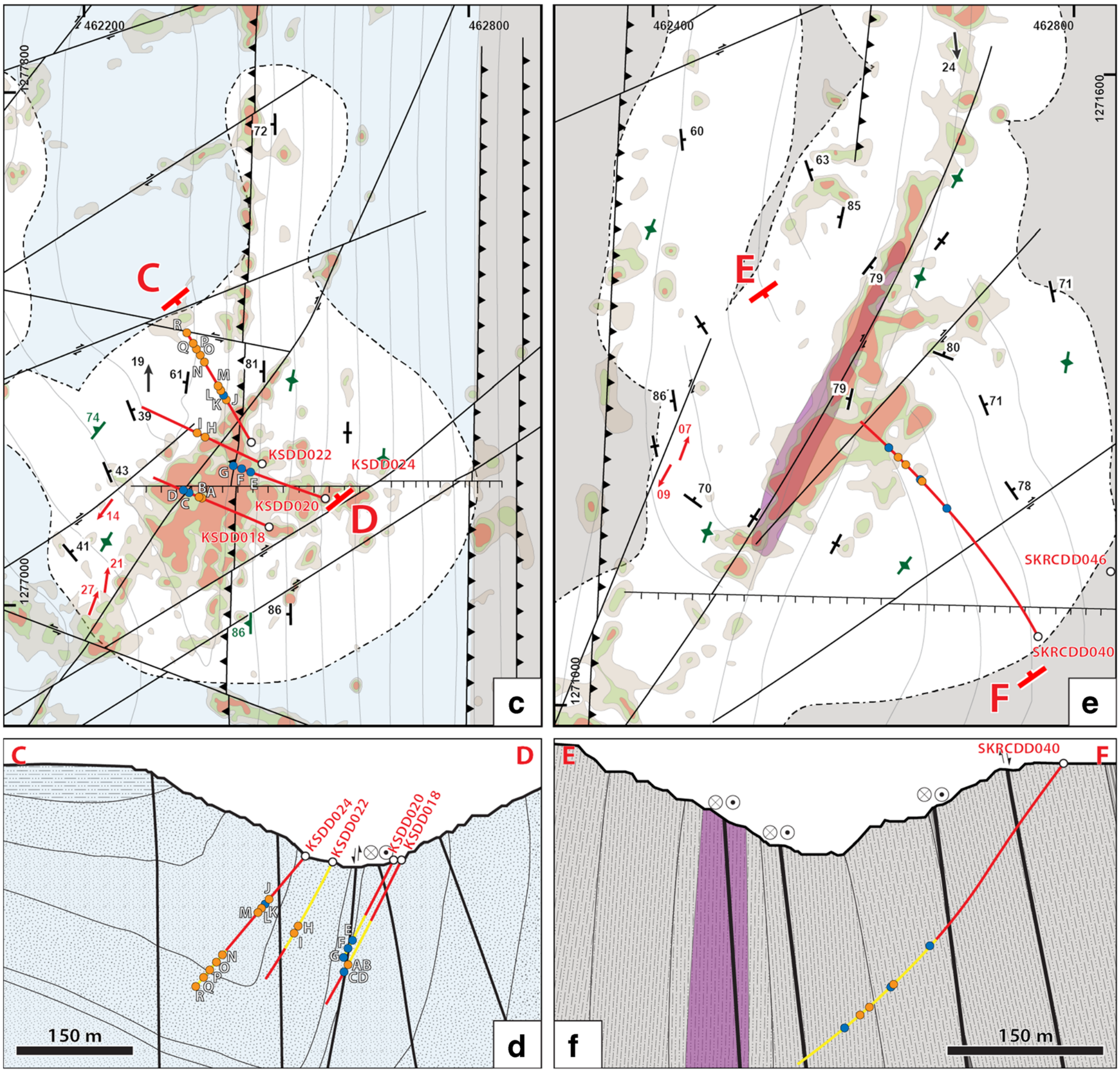


**Fig. 4** (continued)

alteration in specimens (e.g. veining, bleaching), the amount of alteration minerals in thin section and gold grades. Sample BD3 was used to normalise the Kintinian conglomerate samples, sample F was used for the Fatoya Formation shale samples, sample O for the Fatoya Formation greywacke samples, sample SK6 for the Balato shale samples and sample SK4 for the Balato greywacke samples. Since no least altered shale and greywacke could be sampled directly in the Kintinian Formation, Kintinian samples BD1 and BD4 were normalised to a sample of shale and greywacke representative of the Siguiri district. The Fatoya Formation samples F and O were therefore chosen for the normalisation of BD1 and BD4, respectively. Variation in an element i between the altered sample and the fresh sample ($=\Delta C^i$) is considered anomalous when its value relative to the least altered sample ($=\Delta C^i/C^i_0$) exceeds ±70 %. Extended methodology about whole-rock geochemistry can be found in ESM 1.

## Results

### Bidini

*Lithostratigraphy and structure*

The Bidini deposit is located in the northern part of the district (Fig. 2). It is hosted by the greywacke-dominated Fatoya Formation and is located east of the contact with the Kintinian Formation (Fig. 4(A, B)). Fatoya Formation sedimentary rocks in the Bidini deposit display various sedimentary features that can be used as way-up indicators, such as cross-bedding, rip-up clasts and ripple marks. Metre-thick beds of medium-grained greywacke and sandstone dominate; however, fine alternations of siltstone and shale can also be occasionally found, as well as some black shale beds. In this deposit, the Fatoya Formation overlies up to 100 m of

**Table 2** Summary table of the detailed geochemical gains and loss of altered samples compared to the least altered samples

| | | | | |
|---|---|---|---|---|
| Samples from | Kintinian conglomerate | Kintinian shale | Kintinian greywacke | Fatoya shale |
| Compared to least altered | Kintinian conglomerate | Fatoya shale | Fatoya greywacke | Fatoya shale |
| Major increase | Au, Bi, Cu, S, Te, W, Zn | Au, Ca, Na, S, Sr, W | Au, Be, Ca, Cs, F, Li, Mg, S, W | Au, As, Bi, Mo, Na, S, Te, W |
| Minor increase | Ba, Cr, K, Li | Mg, Pb, Sb | | Ag, Ca, Cu, Sr |
| Minor decrease | As | | | Ba, K, Rb, Zn |
| Major decrease | | Ba, Cu, K, Rb | Cu, Mo | |
| Samples from | Fatoya greywacke | Balato shale | Balato greywacke | |
| Compared to least altered | Fatoya greywacke | Balato shale | Balato greywacke | |
| Major increase | Ag, Au, As, Bi, S, Te, W | Au, As, Cr, Cu, Na, Ni, Sc, Te, V, W | Au, As, Ca, Pb, S, Te | |
| Minor increase | Co, Mo, Na, Sb | Bi, Co, Ge, Mg, Sr | Sb, Sr, Zn | |
| Minor decrease | Ba, K, Mg, Rb, Tl, Zn | | Cu | |
| Major decrease | | Mo, P, Pb, S | | |

conglomerate interbeds, intersected in core BDRCDD009 (Fig. 4(A, B) and 5). These conglomerates are part of the younger Kintinian Formation and occur in the Sanu Tinti deposit (Fig. 2). They are separated from the Fatoya Formation sedimentary rocks by a moderately dipping NNE-striking reverse fault (Fig. 6f). The conglomerate interbeds are polymict, clast-supported and interpreted to be the product of repeated subaqueous debris flow events (Fig. 6e; Lebrun et al. 2015b).

In the Bidini deposit, bedding strikes N-NE on average with multiple small-scale open $F_{2S}$ folds. The deposit is located on the hinge of a refolded $F_{2S}$ anticline the fold axes of which plunge shallowly to the north and south (Fig. 2 and 4(A)). The $F_{2S}$ folds are crosscut by multiple early-$D_{3S}$ subvertical incipient structures oriented NE-SW and N-S (Fig. 6a). These incipient structures are mainly developed in the centre of the deposit and are expressed as discreet fracture zones associated with areas about 10 m wide where the density of mineralised $V_{3B}$ veins increases (Fig. 6b; Lebrun et al. 2015a). These fracture zones are open at depths of up to 300 m (Fig. 4(A, B)). Veining in Bidini is dominated by the $V_{3B}$ vein set (Fig. 6b, c) and some $V_{3A}$ veins. In drill core, $V_{3A}$ veins commonly have brecciated structures and range in width from a few millimetres up to 20 cm. In comparison, individual $V_{3B}$ veins typically have antitaxial textures (Passchier and Trouw 2005) and are only a few centimetres to 15 cm thick but can extend for up to tens of metres. Supergene alteration has formed a centimetre-wide halo of iron oxides around the $V_{3B}$ veins, preserving them from further weathering (darker zone around quartz vein in Fig. 6c).

*Mineral assemblages and mineralisation*

Hydrothermal mineral assemblages in the Bidini deposit display contrasted styles of mineralisation dependant on the host lithology. In the greywacke or shale beds of the Fatoya Formation, hydrothermal activity formed mineralised veins whereas in the conglomerate of the Kintinian Formation, hydrothermal alteration is disseminated throughout the matrix and clasts of the conglomerate (Fig. 3d).

In the Fatoya Formation, mineralisation is controlled by early-$D_{3S}$ N-S and NE-SW fracture zones, around which $V_{3S}$ veining develops. Both the $V_{3A}$ and the $V_{3B}$ vein sets were found in Bidini. The $V_{3A}$ carbonate-pyrite veins show coeval growth of pyrite and minor arsenopyrite. Carbonate in $V_{3A}$ veins is dominantly ankerite, and these veins are commonly found associated with a halo of siderite grains overprinting metamorphic sericite. Minor albite can also be found in this vein set. Free gold occurs along fractures in $V_{3A}$ pyrite and is associated with chalcopyrite and galena. The $V_{3B}$ veins typically have rims of ankerite and a core of quartz and are associated with sulphides. These sulphides are typically located along the selvages or disseminated as haloes of up to a metre thick around the veins, where arsenopyrite is dominant. However, a halo of pyrite can be found instead of, or accompanying, the arsenopyrite crystals. Pyrite associated with $V_{3B}$ veins can occasionally be observed as pseudomorphs after siderite in the albitised host rock (Fig. 7a). In drill core, each vein is typically associated with carbonate alteration of up to a few metres away from the vein and expressed as bleaching, usually related to Fe-oxides coming from the oxidation of ankerite and/or by millimetre-sized siderite grains. The mineralised fracture zones, highlighted by the $V_{3B}$ veins, therefore form widespread siderite-ankerite alteration haloes of up to 100 m width (e.g. BDRCD009; Fig. 5). Native gold is found in the quartz or at the contact between quartz and ankerite in the $V_{3B}$ veins. Free gold can also be found in $V_{3B}$ arsenopyrite fractures, in association with chalcopyrite and galena (Fig. 7b). The $V_{3B}$ veins are overprinted and folded by the $S_{4S}$ cleavage (Fig. 6c), which commonly develops strain shadows of pyrite, chalcopyrite, quartz and ankerite around the $V_{3B}$ arsenopyrite (Fig. 7e). Pyrite and

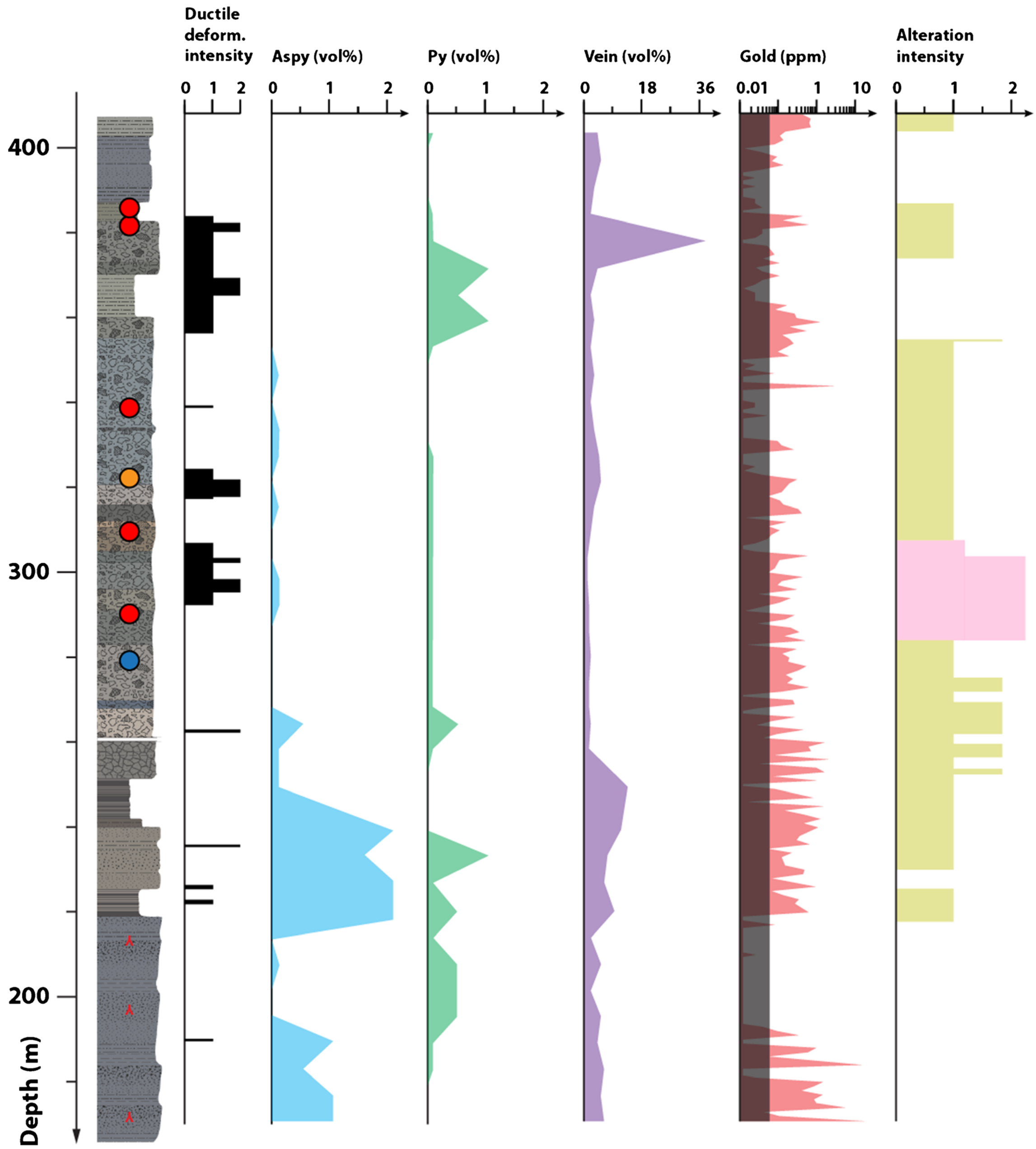


**Fig. 5** Log of hole BDRCDD009 from the Bidini and Sanu Tinti deposits (location map on Fig. 3). The log has been overturned to account for the stratigraphy, the Kintinian formation being younger than the Fatoya formation (Lebrun et al. 2015b). The alteration intensity section displays carbonate alteration in *light brown* and albitisation in *light pink*. Way-up indicators (*Y*) in *red* are based on graded bedding ripple marks and rip-up clasts. Position of the collected samples reported as *coloured discs* (conglomerate samples in *red*, shale in *blue* and greywacke in *orange*). Deformation intensity scaled arbitrarily from 0 (no deformation) to 1 (moderate deformation) and 2 (intense deformation). Background level for Au is represented by a *shaded area*. Lithology as in Fig. 4

chalcopyrite can also be found along the $S_{4S}$ penetrative cleavage (Fig. 6d).

Hydrothermal mineral assemblages in the underlying Kintinian Formation conglomerate have very distinct textures. The gold-bearing mineral assemblage is dominated by disseminated sulphides, largely pyrite, developed along the NNE-striking hanging wall of the conglomerate and exhibits little to no $V_{3B}$ veining (Fig. 3d). Minor tourmaline, chalcopyrite and gold are associated with disseminated pyrite. Free gold was commonly found as inclusions or within fractures in pyrite and associated with chalcopyrite (Fig. 7c). Gold-bearing pyrite is cut across by, or has strain shadows of, chalcopyrite, hematite and chlorite (Fig. 7d). The hematite-chlorite association was also found with magnetite (pseudomorphosed by pyrrhotite) and titanite (also pseudomorphosed by pyrrhotite). High-grade mineralisation zones are associated with pyritisation, carbonate alteration dominated by ankerite and intense albitisation.

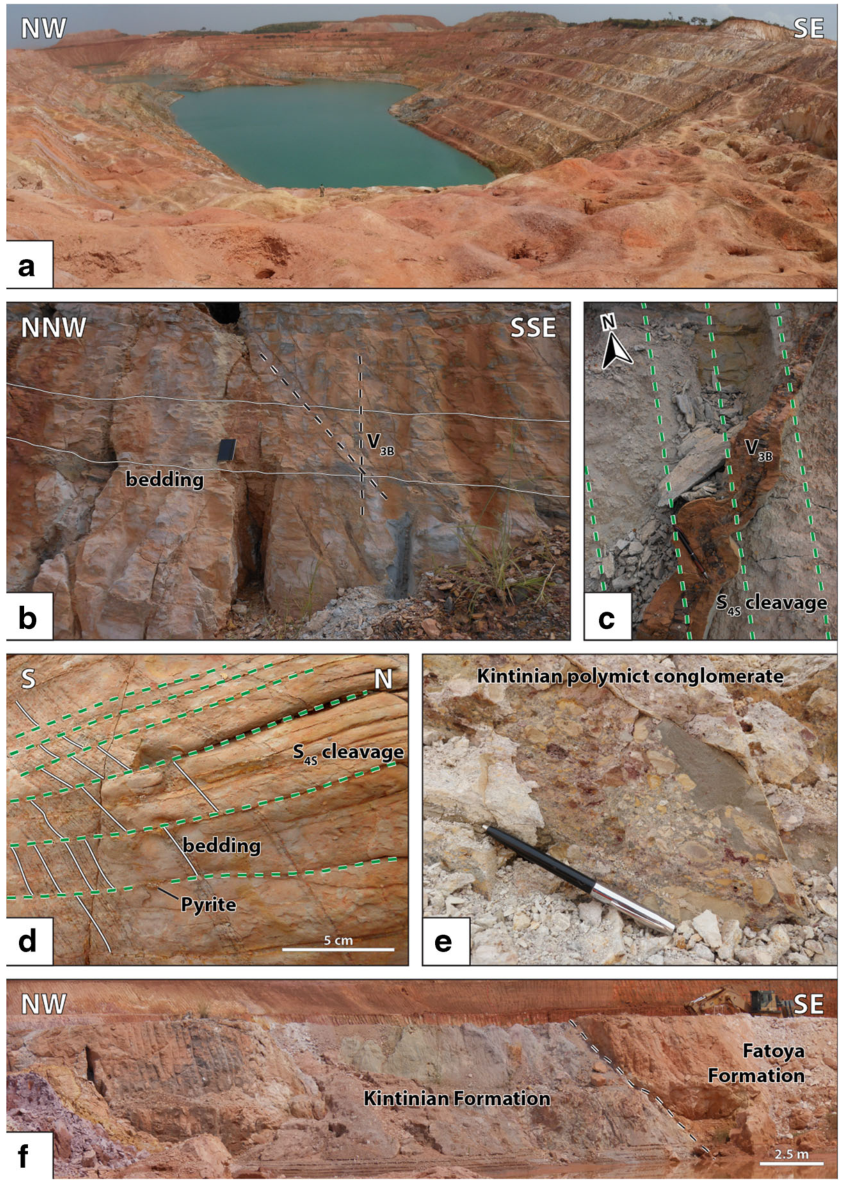


**Fig. 6** Photographs of the main structural elements from the Bidini and Sanu Tinti deposits. **a** Overview of the Bidini deposit. In the foreground, 5- to 20-m-deep holes dug by local villagers are used to reach $V_{3B}$ veins in one of the NE-SW-trending high-grade zones along which the deposit sits. A second high-grade zone is visible on the *right* (just below the *SE* symbol). **b** Conjugate relationships between $V_{3B}$ veins. **c** Folded $V_{3B}$ vein and axial planar $S_{4S}$ cleavage. **d** Pyrite developed along the $S_{4S}$ cleavage. **e** Close-up photograph of the polymict conglomerate from the Kintinian Formation found below the Bidini deposit and in the Sanu Tinti deposit. **f** Structural contact (fault) between the Kintinian and Fatoya formations in the Sanu Tinti deposit

## Sintroko PB1

### *Lithostratigraphy and structure*

Sintroko PB1 is one of the southernmost deposits of the Siguiri district and is hosted by the Balato Formation (Fig. 2). Rocks at Sintroko PB1 consist of centimetre- to decimetre-thick beds of shale-siltstone interlayered with medium- to fine-grained greywacke and sandstone beds. A distinctive 10- to 20-m-thick black shale bed can be followed through the centre of the deposit (Fig. 4(E, F) and 8a). Bedding is sub-vertical in this deposit. In the central black shale area, bedding is oriented NNW-SSE whereas the eastern and western sides of the deposit show open $F_{2S}$ folding with sub-vertical fold axes. Isoclinal $F_{2S}$ folds with vertical fold axes are also commonly observed (Lebrun et al. 2015a). The $F_{2S}$ folds are associated with bedding-parallel $V_{2S}$ veins typically ~5 cm thick and locally up to tens of centimetres thick. These veins can extend over several tens of metres along bedding. En-echelon $V_{2S}$ veins in Sintroko PB1 are commonly thinner than the bedding-parallel variation in $V_{2S}$, and rarely exceed 4 cm in thickness. In cross section, en-echelon vein arrays extend over 2–3 m, but individual veins typically extend for a maximum of 50 cm only. The $F_{2S}$ folds and associated $V_{2S}$ veins are crosscut by an early-$D_{3S}$ NE-striking sub-vertical shear zone sub-parallel to the central black shale unit (Fig. 4(E, F)). This shear zone, the most visible structural element in the deposit, is accompanied by two other sub-vertical NE-SW fracture zones that cut across bedding. These fracture zones exhibit an increased density of veins (Fig. 8b, c). The veins associated with

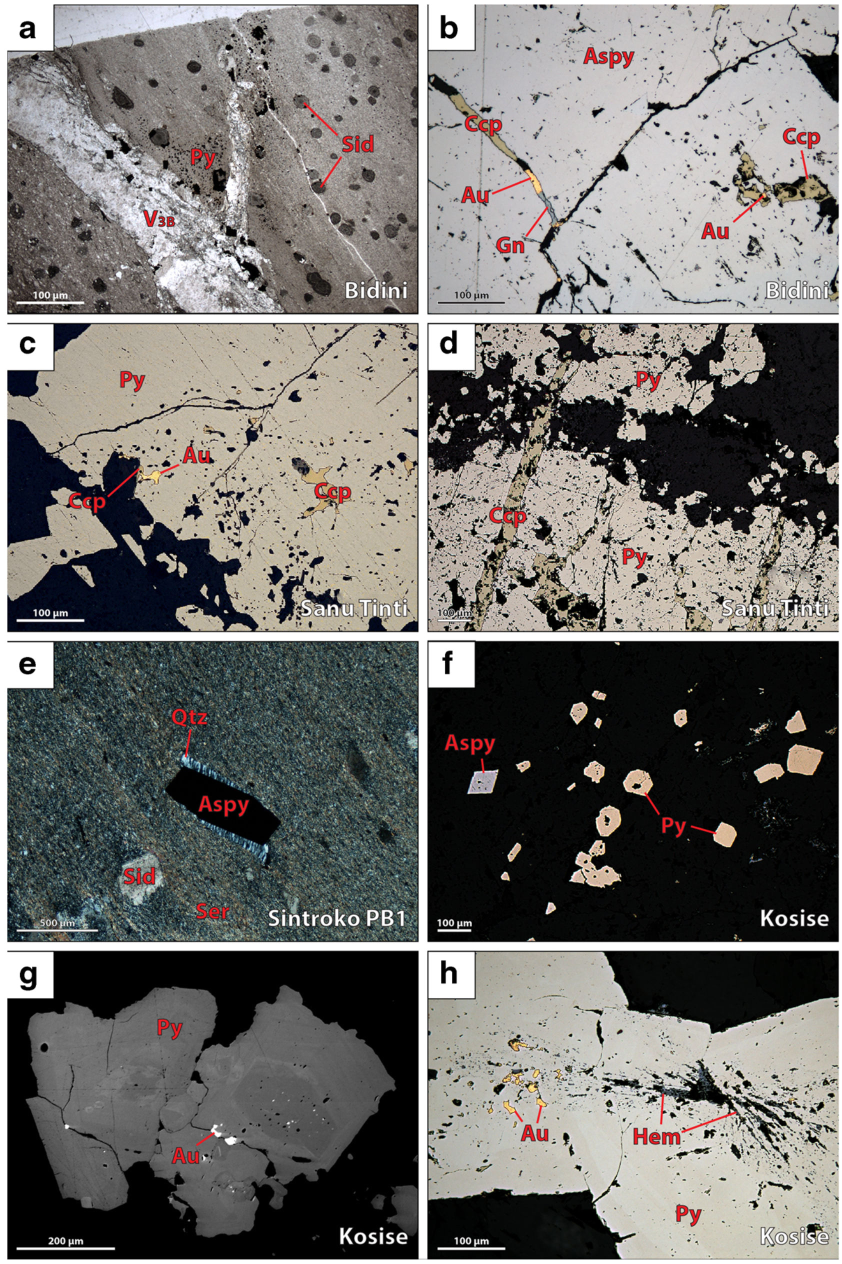


**Fig. 7** Photomicrographs of **a** siderite grains being pseudomorphosed by $V_{3B}$ pyrite; **b** Fractured arsenopyrite in a $V_{3B}$ vein showing gold-chalcopyrite-(galena) infills; **c** Disseminated $V_{3B}$ pyrite fractured and showing gold-chalcopyrite infills; **d** Sanu Tinti style $V_{3B}$ pyrite overprinted by chalcopyrite veinlets; **e** $V_{3B}$ arsenopyrite showing quartz strain fringes associated with the development of the $S_{4S}$ penetrative cleavage. This cleavage is also responsible for the preferential orientation of the sericite and the strain shadows developing around the siderite grains; **f** Textural similarities between $V_{3A}$ pyrite and arsenopyrite suggesting their coeval development; **g** backscattered electron image of $V_{3A}$ pyrite displaying As-rich and As-poor growth rings and being cut by gold infilled fractures; **h** hematite inclusions in $V_{3A}$ pyrite associated with gold. Hematite laths seem to follow the pyrite crystal lattice whereas gold displays triangular textures typical of open space infill (Taylor 2010). *Aspy* arsenopyrite, *Au* gold, *Ccp* chalcopyrite, *Gn* galena, *Hem* hematite, *Py* pyrite, *Qtz* quartz, *Ser* sericite, *Sid* siderite

these incipient structures are dominated by the $V_{3B}$ vein set, and no $V_{3A}$ veins were observed in Sintroko PB1. The $V_{3B}$ vein set commonly has conjugate geometries characterised by NE-SW striking veins dipping either moderately to the SE or steeply to the SE or the NW (Fig. 8f).

*Mineral assemblages and mineralisation*

The hydrothermal mineral assemblages in Sintroko PB1 are hosted in the veins developed in and around the NE-SW shear zone sub-parallel to the central black shale layer (Fig. 4(E, F)) and NE-SW fracture zones. Veining becomes more prominent in more competent units, such as greywacke, and is refracted in shale beds (Fig. 8d). The $V_{2S}$ veins consist of quartz and minor ankerite. Free gold is hosted within $V_{3B}$ quartz-ankerite-sulphide veins and located in the quartz core of the veins or at the contact between the quartz and the ankerite rims. Arsenopyrite, developed in and around the $V_{3B}$ veins (Fig. 8e), is the main sulphide phase in shale beds whereas pyrite becomes more common in greywacke and sandstone beds. In drill core, high-grade mineralised zones are typically associated with a carbonate alteration halo characterised by disseminated millimetre-sized siderite grains, ankerite and extending up to a couple tens of metres across (e.g. SKRCDD040; Fig. 9). Sericite is developed mainly along

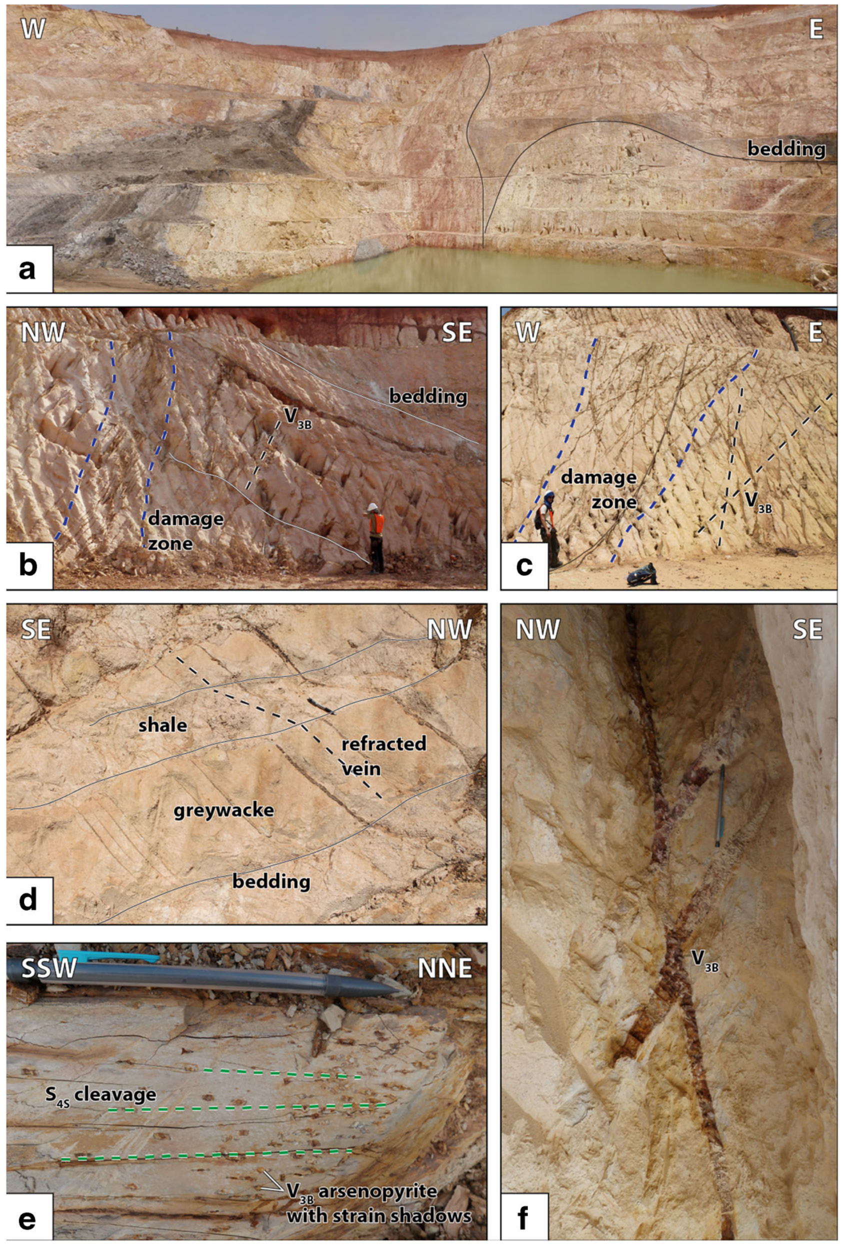


**Fig. 8** Photographs of the main structural elements found in the Sintroko PB1 deposit. **a** Overview of the deposit. The main ore shoot found in this deposit follows the black shale layer (*left*) and cuts across the $F_{2S}$ sub-vertical fold found on the eastern side of the deposit (*right*). **b** Photograph of an ore shoot, expressed as a sub-vertical fracture zone (*area between blue dashed lines*) associated with dense $V_{3S}$ veining. **c** Another example of a fracture zone (*area between blue dashed lines*) associated with high gold grades and of the large-scale conjugate geometry displayed by the $V_{3B}$ veins. **d** Refraction of $V_{3B}$ vein orientations between beds of greywacke and shale. **e** Strain shadows around arsenopyrite crystals developed around a $V_{3B}$ vein (crumbled down on the *right*) by the $S_{4S}$ cleavage. **f** Conjugate relationship of the $V_{3B}$ veins at the outcrop scale

the $S_{4S}$ cleavage, and pyrrhotite, chalcopyrite and quartz can be found in the strain shadows around $V_{3B}$ arsenopyrite (Fig. 7e and 8e).

## Kosise

### *Lithostratigraphy and structure Kosise*

The Kosise deposit is hosted by the Fatoya Formation and is located to the west of the contact with the Balato Formation (Fig. 2). Sedimentary beds in Kosise are typically a metre thick and commonly display sedimentary features, such as graded bedding, ripple marks, rip-up clasts as well as loading and cross-bedding structures. These sedimentary features were used as way-up indicators and show that the Fatoya Formation in this deposit is normally graded. Kosise lithostratigraphy is dominated by beds of medium- to coarse-grained greywacke, and some beds of sandstone can also be found in the north of the deposit in addition to rare alternations of thin siltstone and shale beds can also be found.

Kosise is located in a $F_{2S}$ syncline oriented N-S with a sub-horizontal fold axis (Fig. 4(C, D)). This open fold has a vergence to the west (Fig. 10a) and presents bedding-parallel and en-echelon $V_{2S}$ veins along both limbs. A number of early-$D_{3S}$ sub-vertical structures cut the $F_{2S}$ syncline, including NE-SW dextral shear zones, a N-S thrust fault developed along the steep limb of the fold and an E-W normal fault (Fig. 10c; Lebrun et al. 2015a). Most of the early-$D_{3S}$

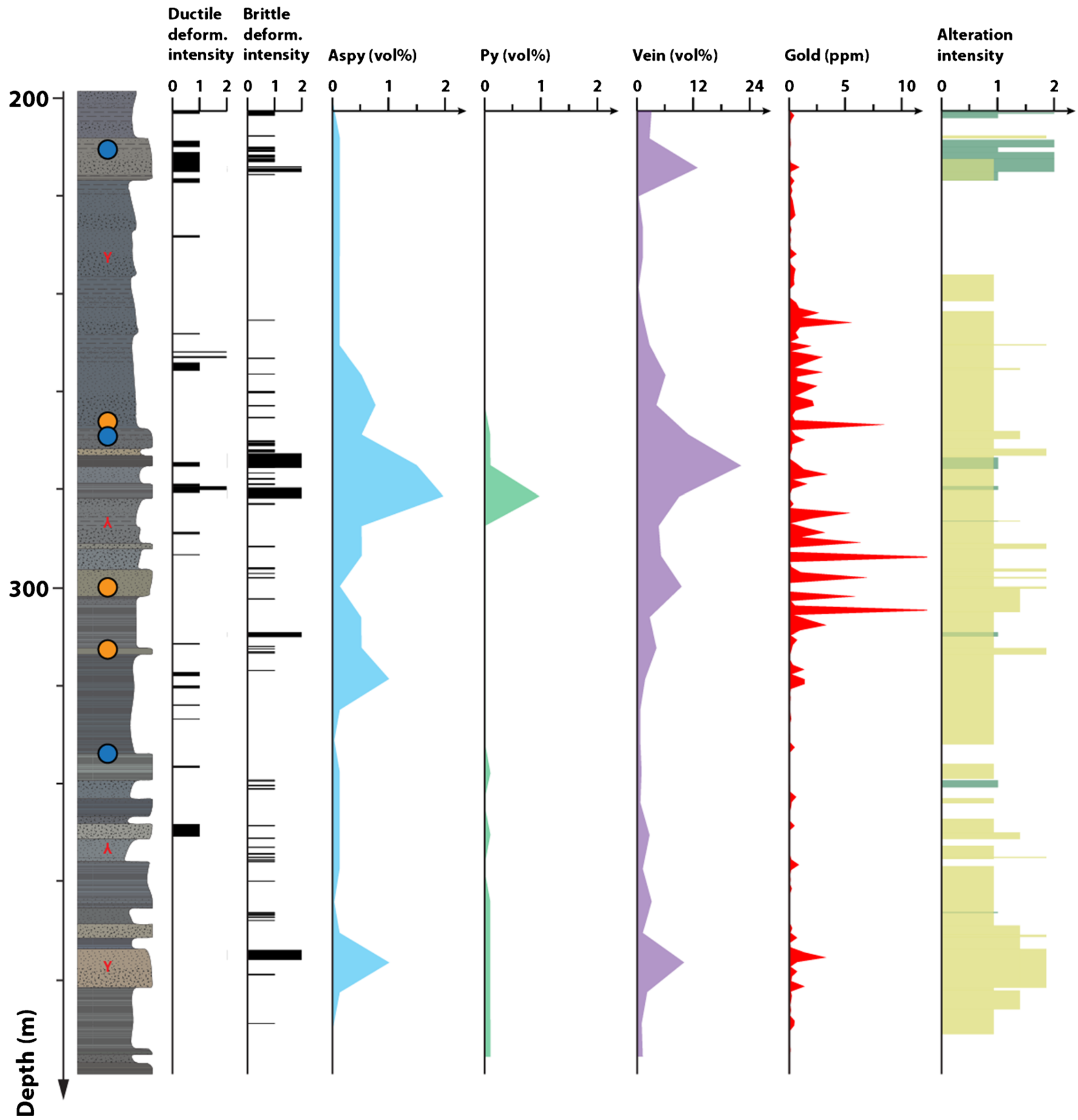


**Fig. 9** Log of hole SKRCDD040 (location map on Fig. 4C). This log highlights the strong link between brittle deformation, veining, sulphidation and carbonate alteration with gold. The alteration intensity section displays carbonate alteration in *light brown* and overprinting chloritisation in *green*. Way-up indicators (*Y*) in *red* are based on graded bedding ripple marks and rip-up clasts. Position of the collected samples reported as *coloured discs* (shale samples in *blue*, greywacke in *orange*). Deformation intensity scaled arbitrarily from 0 (no deformation) to 1 (moderate deformation) and 2 (intense deformation). Lithology as in Fig. 4

structures present in this deposit are fracture zones and incipient faults, highlighted only by the increase in vein density developed late-$D_{3S}$ in the first 10 to 15 m around them (Fig. 10b). The two different $V_{3S}$ vein sets ($V_{3A}$ and $V_{3B}$) were observed around the fracture zones, both in the field and drill core. The $V_{3A}$ vein set develops in the first few metres of the fracture zones whereas the $V_{3B}$ vein set commonly extends up to 15 m across. In the Kosise deposit, the orientation of $V_{3A}$ veins is extremely variable with individual veins showing brecciated textures. In contrast, $V_{3B}$ veins are conjugate and oriented around 150/40 and 145/70, with common antitaxial textures (Fig. 3g).

*Mineral assemblages and mineralisation*

The XRD analyses on the Kosise Formation samples show that the host greywacke comprises >40 vol% albite, 7 vol% carbonate (calcite vol% + ankerite vol% + siderite vol%), >5 vol% chlorite (chamosite), 15 vol% white mica and 27 vol% quartz. In shale beds, chamosite and white mica increase to 8 and 28 vol%, respectively, and quartz decreases to 17 vol%. These abundances vary by only a few percent across the ore shoots (ESM 2 Table 1). The $V_{2S}$ en-echelon veins cut the already albitised and sericitised host rock. In Kosise, these veins are dominated by quartz with rare ankerite

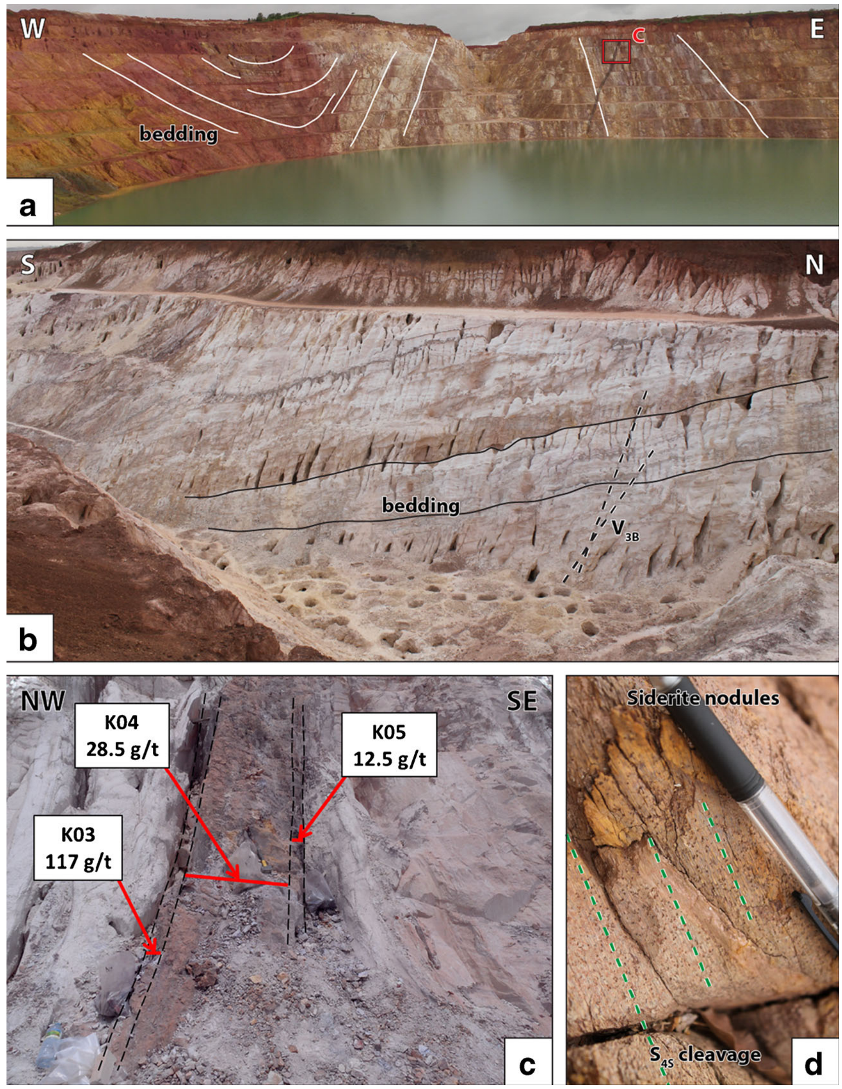


**Fig. 10** Photographs of the main structural elements found in the Kosise deposit. **a** Overview of the deposit. The northern part of the deposit (centre) hosts a bedding parallel thrust fault that develops intense $V_{3S}$ veining (**b**). **b** Veining developed in the northern part of the deposit. The $V_{3B}$ veins are stratigraphically controlled and mainly hosted in the greywacke and sandstone beds. **c** Close-up photograph of one of the rare discrete structures controlling gold grades in the Siguiri district, a dextral NE-SW shear zone. Gold grades across this shear zone are over 100 g/t Au. **d** Siderite grains developed around the ore shoots. The sub-vertical $S_{4S}$ cleavage overprints these grains

and albite. No free gold was observed in $V_{2S}$ pyrite. The rest of the hydrothermal mineral assemblages in the Kosise deposit are controlled by the N-S, NE-SW and E-W structures. The deposit is located at their intersection (Fig. 4(C, D)), and gold grade within some of the shear zones can be greater than 100 g/t (Fig. 10c). Similar to Sintroko PB1, vein distribution is also partly controlled by the host rock rheology, with veining becoming more abundant in more competent units (Fig. 10b). Artisanal miners primarily excavate the $V_{3B}$ veins and ignore the $V_{2S}$ and $V_{3A}$ vein sets. However, petrography confirms that both $V_{3A}$ and $V_{3B}$ vein sets carry gold. Ankerite-pyrite $V_{3A}$ veins show the early to coeval growth of minor arsenopyrite along with pyrite (Fig. 7f), and SEM imaging coupled with qualitative EDS on $V_{3A}$ pyrites shows As zoning (Fig. 7g) and rare monazite inclusions, less than 20 μm in diameter. Gold in the $V_{3A}$ pyrite is located in fractures or as inclusions with triangular textures, characteristic of infill (Taylor 2010). Gold is associated also with chalcopyrite and hematite (Fig. 7h). As in all other deposits, sulphides associated with $V_{3B}$ veins change according to the host lithology with arsenopyrite dominating in shale beds and the proportion of pyrite increasing in greywacke and sandstone beds. Alteration around the ore shoots is characterised by carbonate alteration haloes associated with bleaching typically due to ankerite oxidation and millimetre-sized siderite grains (Fig. 10d).

## Whole-rock geochemistry

### *Baseline geochemistry*

Baseline geochemistry from each of the three formations hosting the Siguiri district displays variations in a suite of elements (background values are reported in ESM 5 Table 4 and some, shown in Fig. 11). In particular, baseline geochemistry of the Kintinian Formation is associated with increased background concentrations of Ca, F, Ga, Li, Mg, Ni, Sc, Sn, Sr, U, V and W and decreased concentrations of As, Cu, Si and

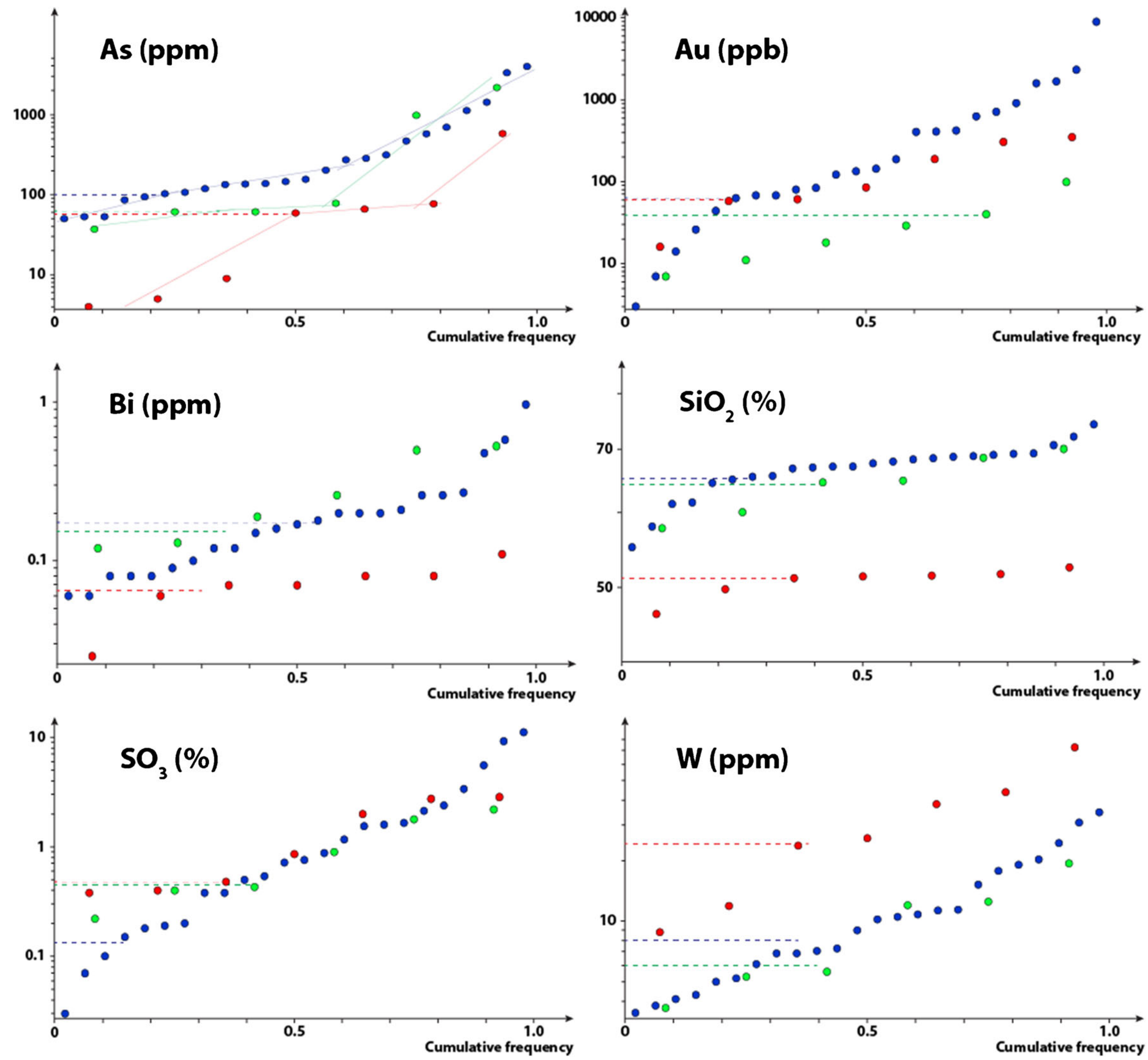


**Fig. 11** Cumulative frequency diagrams for As, Au, Bi, $SiO_2$, $SO_3$ and W. The datasets are separated by hosting formation (Kintinian in *red*, Fatoya in *blue* and Balato in *green*). The first inflexion in each dataset represents the background threshold (marked by a *dotted line*) and the beginning of the influence of anomalous concentrations. Adapted from lognormal cumulative frequency diagrams of Landry (1995)

Zr when compared to the Fatoya and Balato formations (Fig. 11; ESM 5 Table 4). Baseline geochemistry of the Balato Formation, when compared to those for the Kintinian and Fatoya formations, is associated with a marked increase in Ba, Be, Zn and Zr; minor increases in concentration of Cu and Th; marked decreases in Au and Sb; and a minor decrease in W (Fig. 11; ESM 5 Table 4). The baseline geochemistry of the Fatoya Formation is associated with increased background concentrations in Na, As, Mo and Te and minor increases in Bi and Si, whereas decreases in Ca, K, Li, S, Sn and Sr can be observed when compared to the Kintinian and Balato formations (Fig. 11; ESM 5 Table 4).

*Geochemical footprint of mineralisation*

Mass balance calculations and comparison between least altered samples and altered/mineralised samples of each rock type and in each formation made it possible to quantify the extent of element enrichment or depletion towards the ore zones (ESM 6 Table 5). Overall, geochemical changes towards the ore shoots are characterised by major increase in Ag, Au, As, Bi, Te and W, accompanied by additional minor increase in Co, Mo, Na/Al (molar), S and Sb and minor decrease in 3K/Al (molar), P, Rb and V, whereas Ca and Mg change widely (Table 2).

In addition to these district-scale geochemical variations between each formation and host rock, high-grade mineralised zones in Kosise (some over 100 g/t Au; Lebrun et al. 2015a) are associated with a geochemical alteration halo at least 15 m wide, characterised by an increase towards the ore shoots in Ag, Au, As, Bi, Co, Mo, Na, S, (Sb), Te and W (Fig. 12 and ESM 6 Table 5). In detail, Au increases from 3 to 8931 ppm, As increases from 50 to 3996 ppm, Bi increases from 0.06 (just above detection limit; =0.05 ppm) to 0.97 ppm, Mo

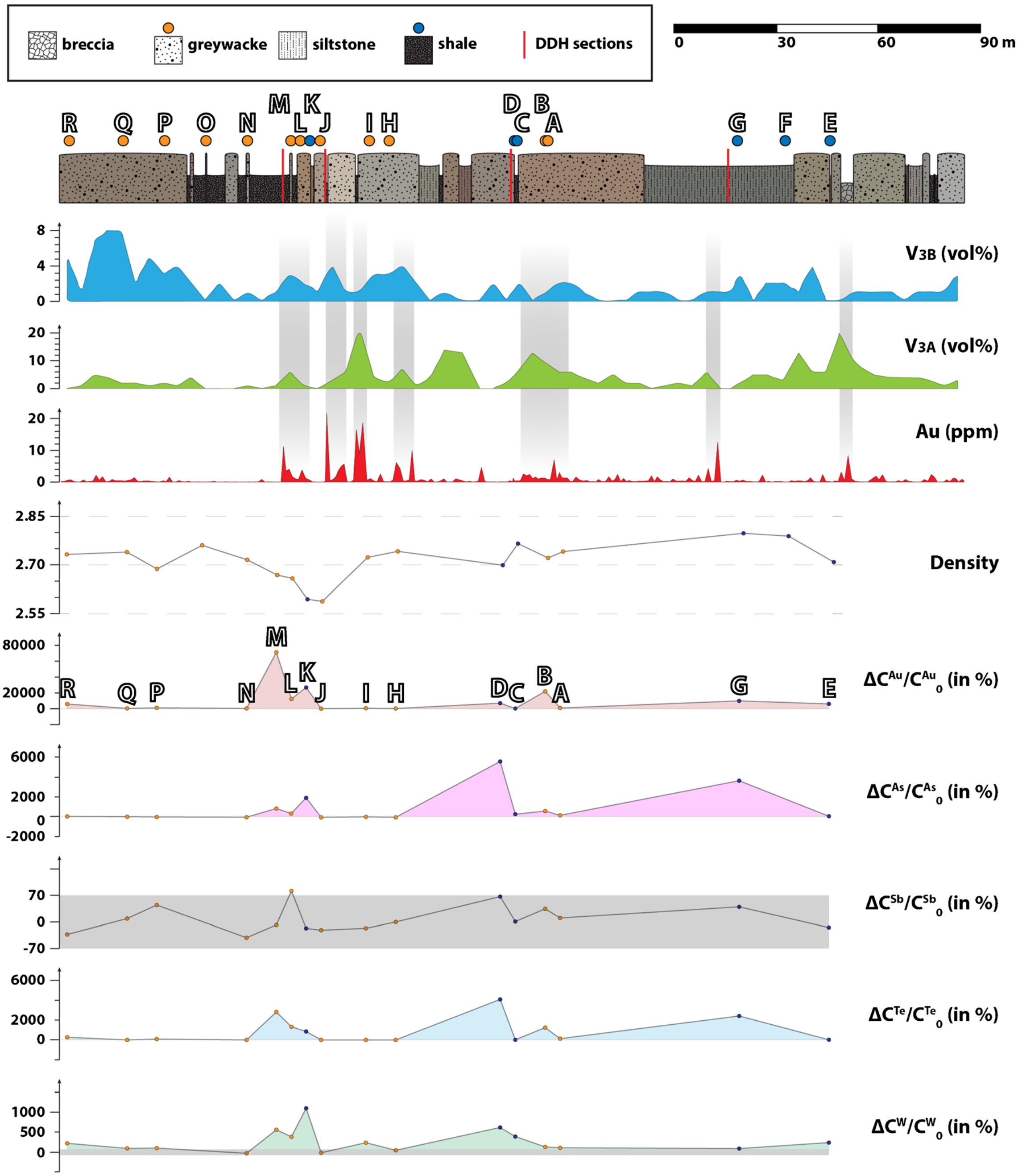


**Fig. 12** Composite log and geochemical cross section from the Kosise deposit. Two mineralised zones were identified (around samples *J*, *K*, *L*, *M* and samples *A*, *B*, *C*, *D*) and are in proximity to shear zones and a thrust fault (Fig. 4C, D, 10A and C). The main mineralised zone (samples *J*, *K*, *L*, *M*) is associated with typical orogenic gold enrichments in Au-As-Sb-Te and W. Mass balance calculations were conducted for each individual sample, and sample *O* and *F* were used as least altered greywacke and shale sample, respectively. The composite geochemical cross sections also show enrichments in Bi, Mo and S around the main mineralised zone (samples *J*, *K*, *L*, *M*). Ca increases away from the main mineralised zone and is interpreted to represent the reaction front. The fact that Si does not show any variation across the ore shoots is attributed to the removal of the veins in each sample (host rock characterisation only). Molar and normalised 3K/Al and Na/Al saturation indices (Kishida and Kerrich 1987) highlight both mineralised zones. Each geochemical sample was normalised to the corresponding greywacke or shale least altered sample (*O* and *F*, respectively). *Shaded areas* represent a 70 % variation in a considered chemical element or species concentration relative to the least altered sample

increases from 0.3 to 2.3 ppm, Sb increases from 0.6 to 3.2 ppm, S increases from 0.06 to 4.47 ppm and W increases from 3.5 to 34.9 ppm. Within the same alteration halo around the ore shoot, Cs, (Li), Mg, (Mn), P, Rb, (Sc), (Tl), (V) and (Zn) decrease (Fig. 12 and data in ESM 6 Table 5). Concentrations of Ca display a peculiar behaviour, increasing a few tens of metres away from the main ore shoot. Silicon in the host rock does not show significant variation, due to the

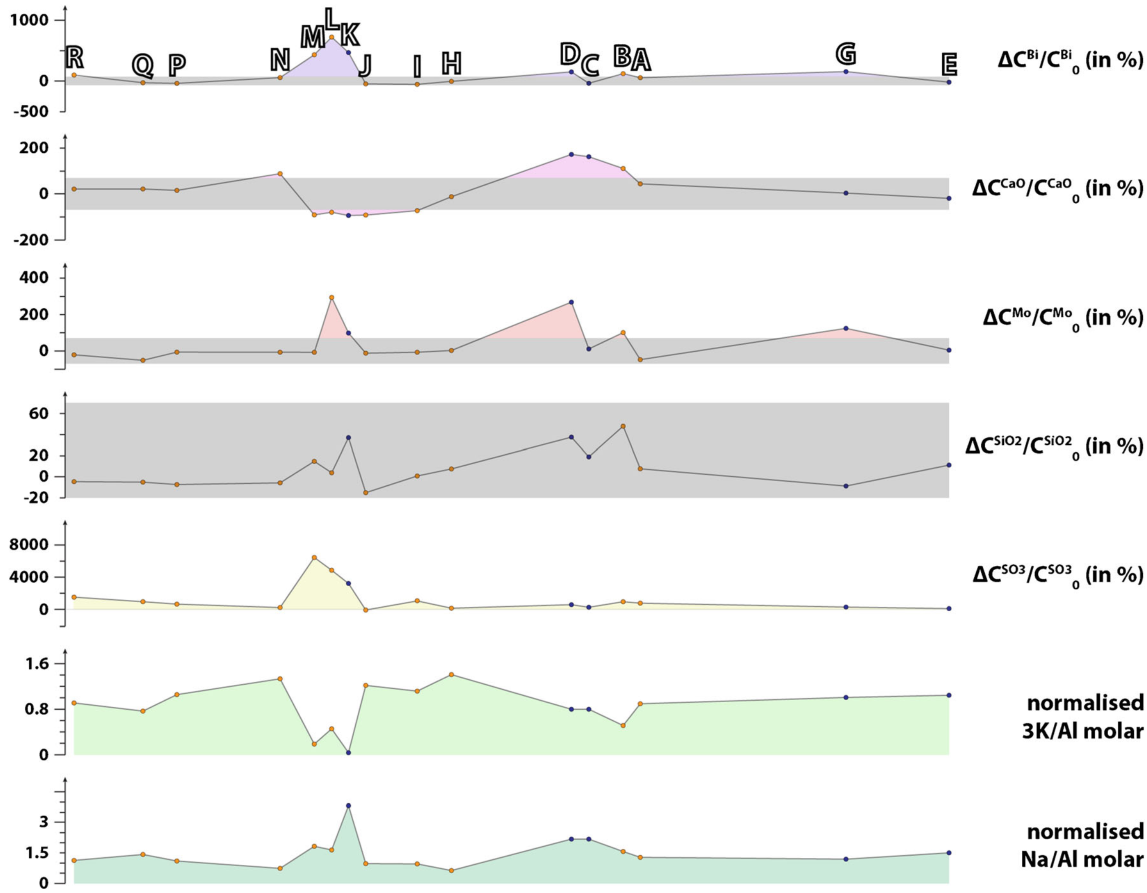


**Fig. 12** (continued)

removal of all veins from the analysed samples. Saturation indices (molar ratios) for muscovite (3K/Al) and albite (Na/Al; Kishida and Kerrich 1987) vary from 0.07 to 0.66 and from 0.26 to 0.84, respectively, and clearly show a respective increase and decrease towards the ore shoots (Fig. 12). Collectively, these results suggest that regardless of the hosting formation or lithology, altered rocks in the Siguiri district are enriched in Ag, Au, As, Bi, Co, Mo, (Sb), S, Te and W.

## LA-ICP-MS and EPMA

### *Pyrite*

Pyrite grains associated with the $V_{2S}$, $V_{3A}$ and $V_{3B}$ vein sets, with the $S_{4S}$ cleavage (syn-$D_{4S}$) and disseminated pyrite hosted in the Kintinian conglomerate, were analysed by LA-ICP-MS. Major and trace element signatures of the $V_{2S}$, $V_{3A}$, $V_{3B}$ and $D_{4S}$ pyrite vary in the Ag-As-Au-Cu-S-Sb-Se-Zr geochemical space (Fig. 13F, G, H and J). Major and trace element signatures of pyrite associated with $V_{2S}$ and $V_{3A}$ veins cluster in the high Ag-As-Au-Sb–low Cu-S-Se-Zr part of this geochemical space whereas $V_{3B}$ pyrite, Sanu Tinti conglomerate pyrite and syn-$D_{4S}$ pyrite major and trace element contents cluster in the low Ag-As-Au-Sb–high Cu-S-Se-Zr part of this space. This clustering, first noticed when plotting pyrite data from greywacke beds from the Fatoya Formation only, was also observed when considering pyrite hosted in all formations, host rocks and deposits (Fig. 13).

Comparison between the major and trace element signatures of pyrite from the Fatoya and Kintinian formations shows variations in Co, ranging from below detection limit to up to 1962.3 ppm in the Fatoya Formation and from below detection limit to 32.6 ppm in the Kintinian Formation. Values for Ni range from below detection limit to 1248 ppm in the Fatoya Formation and from below detection limit to 57 ppm in the Kintinian Formation. Values for Cu range from below detection limit to 3688 ppm in the Fatoya Formation, to 2 and 4393 ppm in the Kintinian Formation. In addition, laser ablation data shows that $V_{3A}$ pyrite hosted in greywacke from the Kosise deposit (Fatoya Formation; Fig. 13a) has gold grades up to 43.3 ppm, whereas the other pyrite generations do not reach grades higher than 3 ppm (the three higher values reported on Fig. 13e were obtained from gold inclusions). In summary, pyrite from the Fatoya Formation is associated with increased concentrations in As, Au, Co and Ni (and minor Bi, Mn) and a depletion in Cr, Cu, S, Si, Sn and Zr when compared to the major and trace element signatures of pyrite

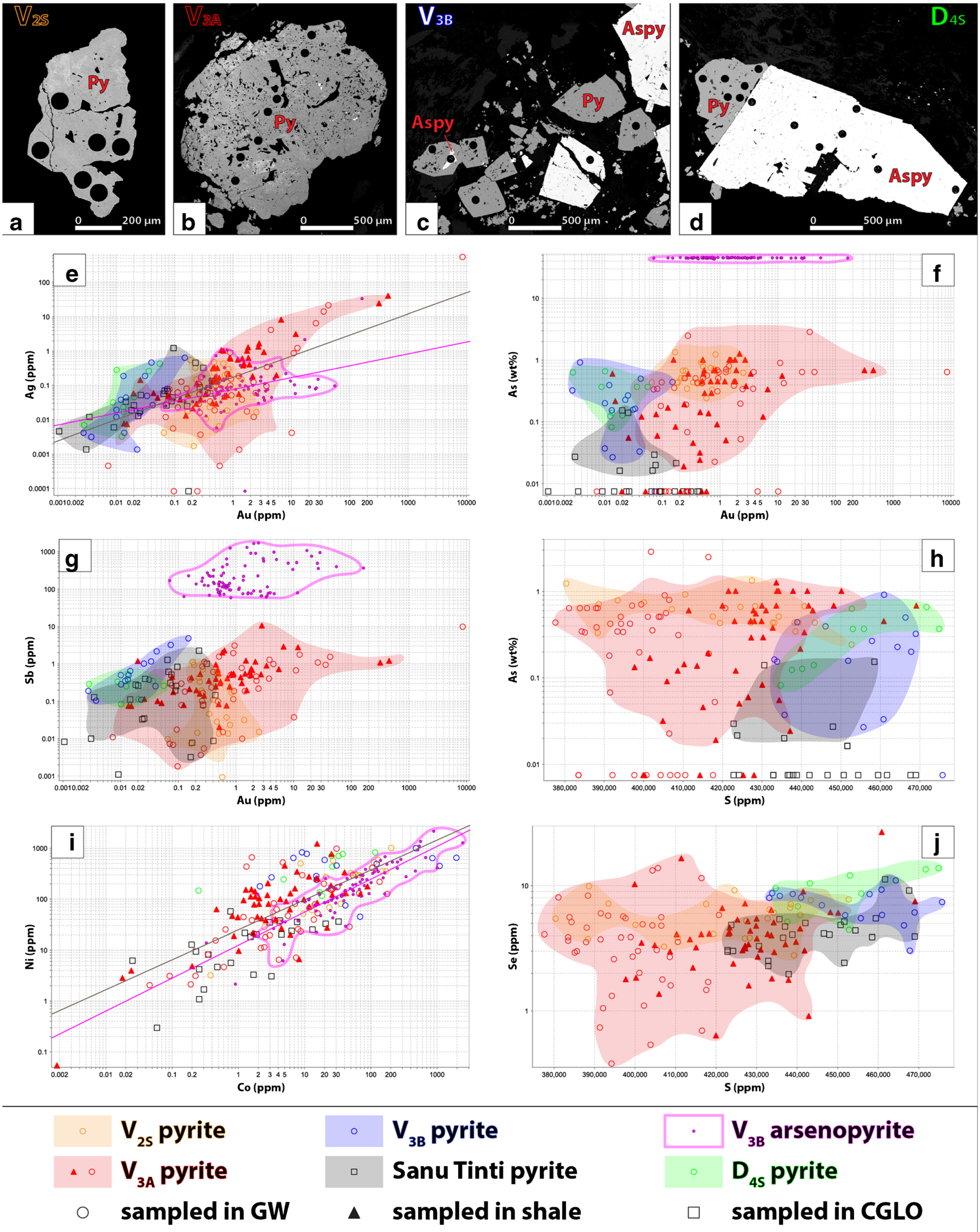
V2S
Py
a
0 200 µm
V3A
Py
b
0 500 µm
V3B
Aspy
Py
Aspy
c
0 500 µm
D4S
Py
Aspy
d
0 500 µm
e
Ag (ppm)
Au (ppm)
f
As (wt%)
Au (ppm)
g
Sb (ppm)
Au (ppm)
h
As (wt%)
S (ppm)
i
Ni (ppm)
Co (ppm)
j
Se (ppm)
S (ppm)
V2S pyrite
V3B pyrite
V3B arsenopyrite
V3A pyrite
Sanu Tinti pyrite
D4S pyrite
sampled in GW
sampled in shale
sampled in CGLO

◀ **Fig. 13** LA-ICP-MS and EPMA data from the different generations of pyrite and arsenopyrite observed in the Siguiri district. These diagrams show that the pyrite compositions for $V_{2S}$ and $V_{3A}$ plot in the same area whereas the other pyrite generations ($V_{3B}$, $D_{4S}$ and Sanu Tinti disseminated pyrite) plot in another area of the diagrams. *Regression lines* are in *black* for pyrite and *pink* for arsenopyrite in *E* and *I*. *GW* greywacke; *CGLO* conglomerate

hosted in the Kintinian Formation (data in ESM 3 Table 2). Moreover, the crystal lattice of the different generations of pyrite shares similar Ag/Au and Ni/Co ratios, around 7.5 and 2.81, respectively (Fig. 13e, i).

*Arsenopyrite*

Arsenopyrite was found associated only with $V_{3B}$ veins. Aside from their differences in major element concentrations, arsenopyrite and all generations of pyrite can also be distinguished when comparing their respective trace element signatures in Bi, Mo, Pb, Sb and Se (and to some extent Co, Cr and Ni). Compared to all generations of pyrite, $V_{3B}$ arsenopyrite is enriched in all these elements (Fig. 13f, g, h, j and ESM 3 Table 2).

Concentrations of As (obtained by EPMA) and Sb vary with Au grades in the samples from the Balato and Fatoya formations, increasing from ~43.2 to ~46.2 wt% As and from ~125 to ~1600 ppm Sb, respectively. Also, $V_{3B}$ arsenopyrite lattice contains significant gold concentrations of up to 55.5 ppm (higher values reported on Fig. 13e were obtained on a gold inclusion). The $V_{3B}$ arsenopyrite has similar Ag/Au and Ni/Co ratios to all pyrite generations, around 7.5 and 2.81, respectively (Fig. 13e and I). In summary, whereas no arsenopyrite was found in the Kintinian Formation, arsenopyrite from the Balato Formation shows enrichment in Ag, Co, Cr, Cu, Sb and Ti (and minor Mn) and depletion in As when compared to the arsenopyrite hosted in the Fatoya Formation (ESM 3 Table 2).

## Discussion

### Polyphase hydrothermal activity and gold mineralisation

Field observations of vein cross-cutting relationships, core logging and petrographic descriptions from Bidini, Sintroko PB1 and Kosise permit the construction of local paragenetic sequences for each individual deposit studied. When compared to one another, the local paragenetic sequences are uniform across the Siguiri district and are characterised by four distinct hydrothermal events. These events were correlated in the district-scale paragenetic sequence (Fig. 14) summarised below. Together, the LA-ICPMS data (Fig. 13) and the general paragenetic sequence of the district reflect the polyphase character of gold mineralisation in Siguiri and three distinct gold mineralisation events were identified.

The mineralogy of the least altered host rock in the Siguiri district is dominated by plagioclase, quartz and shows moderate to intense sericitisation and albitisation. Minor biotite and chlorite, possibly detrital, were also found in the host rock mineral assemblage as well as numerous detrital zircons.

The first hydrothermal event occurred during $D_{2S}$ E-W compression and is characterised by the development of bedding-parallel and en-echelon $V_{2S}$ quartz-(ankerite) veins. The $V_{2S}$ veins are associated with minor albite, sericite, pyrite and traces of rutile. These veins do not present significant gold mineralisation and show little development of alteration around their margins.

The second hydrothermal event occurred late during $D_{3S}$ NNW-SSE transtension and is represented by $V_{3A}$ ankerite-pyrite-(albite) brecciated veins that cut the $V_{2S}$ veins. The $V_{3A}$ veins represent the most proximal expression of $V_{3S}$ veining developed along the early-$D_{3S}$ N-S, NE-SW, WNW-ESE and E-W fracture zones. The $V_{3A}$ veins developed in the core of the sub-vertical structures controlling gold mineralisation. $V_{3A}$ veins are associated with minor sericite, quartz, chlorite, rare monazite and arsenopyrite, pyrrhotite and late chalcopyrite and sphalerite, found in the altered host rock and occasionally in the veins themselves. $V_{3A}$ veins are also characterised by a halo of carbonate alteration and pyritisation. Carbonate alteration is expressed as millimetre-sized siderite grains and bleaching of the host rock typically due to Fe-oxides produced from the oxidation of pervasively developed ankerite (Eilu et al. 1999). The $V_{3A}$ vein set also represents the first episode of gold mineralisation recognised in the Siguiri district. Gold was found incorporated in the $V_{3A}$ pyrite crystal lattice (up to 43.3 ppm Au; Fig. 13; ESM 3 Table 2).

The third hydrothermal event also occurred late during $D_{3S}$ and developed along the 10- to 15-m-thick sub-vertical fracture zones formed early during $D_{3S}$ deformation. This event is mainly characterised by intense $V_{3B}$ quartz-ankerite-arsenopyrite veins and is ubiquitous in the Siguiri district. The conjugate $V_{3B}$ veins moderately to steeply dip to the SE and are associated with minor albite and pyrite. This vein mineralisation is also characterised by minor sericitisation and carbonate alteration mainly expressed as millimetre-sized siderite grains. The third hydrothermal event is also represented by a distinct disseminated texture, only observed in the Bidini and Sanu Tinti deposits. The disseminated mineralisation texture found in the Kintinian polymict conglomerate is represented by disseminated pyrite, accompanied by tourmaline, rare monazite and traces of late chalcopyrite, sphalerite, hematite and ilmenite. Minor sericitisation and carbonate alteration is also associated with this disseminated mineralisation texture. This disseminated mineralisation shows some degree of structural control (Kintinian-Fatoya

**Fig. 14** Paragenetic sequence for the Siguiri district

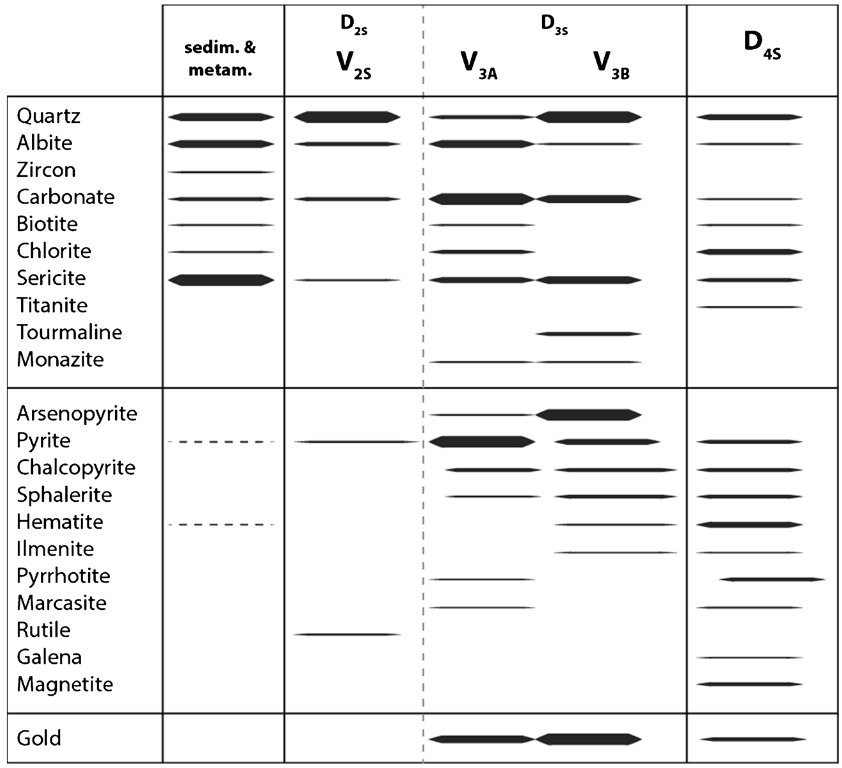


N-S thrust contact) but is mainly stratigraphically controlled by the Kintinian conglomerate. Comparison of major and trace element signatures by LA-ICP-MS and EPMA between the disseminated pyrite and the other generations of pyrite associated with $D_{2S}$, $D_{3S}$ and $D_{4S}$ deformation indicates that the Sanu Tinti disseminated pyrite presents geochemical affinities with $D_{3S}$ and $D_{4S}$ pyrite associated with the $V_{3B}$ veins and the $S_{4S}$ cleavage, respectively (Fig. 13). Since petrographic observations indicate that the Sanu Tinti disseminated pyrite is overprinted by the $S_{4S}$ cleavage, we propose that both $V_{3B}$ and Sanu Tinti disseminated pyrite formed coevally late during $D_{3S}$. Both the vein-hosted and disseminated mineralisation textures developed along the early-$D_{3S}$ N-S thrust at the contact between the Kintinian and the Fatoya Formation. The change between the vein and disseminated mineralisation texture is common in orogenic gold deposits (Groves 1993; Bierlein and Maher 2001; Dubé and Gosselin 2007) and interpreted to be linked to porosity and competency contrasts in Siguiri, where the Kintinian conglomerate has higher porosity and lower competency compared to the greywacke-dominated sedimentary rocks of the Fatoya Formation. The second and main episode of gold mineralisation identified in Siguiri was found to be associated with both the vein-hosted and disseminated mineralisation textures. In the $V_{3B}$ vein-hosted mineralisation, gold was found in the veins and in the lattice of the arsenopyrite crystals (up to 55.5 ppm Au; Fig. 13; ESM 3 Table 2). In the disseminated pyrite, gold was found free along fractures associated with chalcopyrite, hematite and galena. The disseminated pyrite, however, contains a maximum of 3 ppm Au (Fig. 13; ESM 3 Table 2).

The last hydrothermal event is a late overprint developed during $D_{4S}$ NW-SE compression and formed the $S_{4S}$ cleavage. This cleavage is characterised by strain shadows of sericite, quartz, ankerite and albite around $V_{3B}$ arsenopyrite crystals. Chlorite, hematite, pyrite, chalcopyrite, pyrrhotite, sphalerite and magnetite can also be found in these strain shadows or in veinlets overprinting the syn-$V_{3B}$ disseminated pyrite in the Kintinian conglomerate. Even though no significant gold was found in syn-$D_{4S}$ pyrite (~3 ppm Au maximum), free gold was observed in both Bidini and Kosise deposits infilling fractures or strain shadow of early mineralised $V_{3B}$ pyrite and arsenopyrite with chalcopyrite, hematite and galena. Two alternative models can be proposed to explain this infill. In the first model, new gold input may be related to the late syn-$D_{4S}$ hydrothermal event. In the second model, gold may have been remobilised during $D_{4S}$, relocating gold in the $V_{3A}$ and $V_{3B}$ pyrite and arsenopyrite crystal lattice into fractures and pressure shadow. Such remobilisation behaviour has been described by a number of authors in recent years (Wilkinson et al. 1999; Large et al. 2011; Cook et al. 2013). The present dataset does not allow concluding in regard to $D_{4S}$ gold occurrence, and further work would be required to assess whether gold remobilisation occurred or not.

## Geochemical footprint of the ore shoots

The alteration associated with the superimposition of all four hydrothermal events was geochemically characterised across the Siguiri district (Figs. 11 and 12). In the different deposits and in the representative Kosise deposit in particular, the geochemical variations associated with this style of mineralisation are characterised by enrichments in Ag, Au, As, Bi, S, (Sb), Te and W within at least 15 m around the ore shoots (Fig. 12). These enrichments are characteristic of hypozonal to mesozonal orogenic gold deposits (Groves et al. 1998; Eilu et al. 1999; Groves et al. 2003) and are usually accompanied, in Siguiri, by additional increases in Co, Mo and Na/Al (molar) and decreases in Ca, 3K/Al (molar), P, Rb and V across the main ore shoot. These variations can be directly related to the hydrothermal mineral assemblage associated with the $V_{3A}$ and $V_{3B}$ gold mineralisation event. In detail, Co is found as a trace element in pyrite and arsenopyrite. The increase in S is related to sulphidation, and the peculiar behaviour of Ca and Mg along the geochemical transect in the Kosise deposit (Fig. 12) is interpreted to mark the carbonate reaction front. The decrease in 3K/Al and increase in Na/Al molar ratios (Eilu and Groves 2001) can both be linked to albitisation developed around the veins, overprinting and replacing the early sericite of the country rock. Decrease in V can also be related to a decrease in micas towards the ore shoot (Bateman and Hagemann 2004). The absence of silica variation across the ore zones is interpreted as linked to the removal of all veins from the analysed samples. This implies that all silica was derived from hydrothermal fluids and none was derived from the surrounding rocks. Together, these geochemical indicators and their variations can assist exploration by highlighting hydrothermal alteration trends and define vectors to mineralisation, altogether increasing the size of the targets (Christie and Brathwaite 2003).

## Mineralising fluids

If we consider that sulphide major and trace element signatures reflect the composition of the mineralising fluid responsible for their formation (Pitcairn et al. 2006), the compositional clustering between $V_{2S}$ and $V_{3A}$ pyrite, on one side, $V_{3B}$ and syn-$D_{4S}$ pyrite on the other side (Fig. 13), suggests that at least two distinct mineralising fluids can be distinguished. The first fluid was responsible for the deposition of $V_{2S}$ and $V_{3A}$ vein mineralisation whereas the second fluid deposited syn-$V_{3B}$ and syn-$D_{4S}$ mineralisation. Two hypotheses can be formulated on the possible origins of the compositional variations between these two fluids.

The first hypothesis involves a unique source fluid (Salier et al. 2005) and the effect of physico-chemical processes to trigger compositional changes and the evolution of this unique source fluid into two distinct mineralising fluids between the $V_{3A}$ and the syn-$V_{3B}$ hydrothermal events. Such changes are typically caused by changes in the fluid-rock or fluid-fluid interactions, such as the modification of the fluid pathway (Voicu et al. 2000) or fluid mixing (Ridley and Diamond 2000; Boiron et al. 2003).

The second hypothesis involves two different source fluids, pumped through the Siguiri district at different times. Change from the first fluid to the second may have been caused by a change of source reservoir or by a change in the fluid source chemistry. In this hypothesis, fluid-rock and fluid-fluid interactions (Heinrich 2007) only play a minor role on the final composition of the two fluids. Further work beyond the scope of this study (e.g. fluid inclusion, stable isotope studies) would be required to potentially characterise the source(s) of these fluids (Ho et al. 1992; Ridley and Diamond 2000; Tomkins 2013).

However, on the basis of the data presented in this paper, some aspects of the fluid chemistry can still be identified, particularly about the role of As. Field observations of arsenopyrite crystallisation in shale beds versus pyrite crystallisation in greywacke beds, and the differences of the geochemical baseline between the Kintinian, Fatoya and Balato formations (average As contents in the Kintinian Formation conglomerate 5 to 10 times lower than in the greywacke and shale of the Fatoya and Balato formations), we suggest that As was not provided by the infiltrating fluid(s) but mainly by the host rock. From the same observations, As is also interpreted to control the crystallisation of arsenopyrite over pyrite by analogy with other studies (Pitcairn et al. 2006; Price and Pichler 2006).

Variations in As content have a direct impact on the unit cell parameters of the pyrite crystal lattice which affects the capacity of this mineral to contain gold (Savage et al. 2000; Large et al. 2011). This hypothesis is highlighted by the covariance in the LA-ICP-MS and EPMA datasets of Au and As in $V_{3A}$ pyrite: more Au is incorporated into the pyrite crystal lattice along with the increase in As (Reich et al. 2005; Fig. 13f). The low As content of the Kintinian Formation is therefore best interpreted to be responsible for the low Au content of the syn-$V_{3B}$ pyrite disseminated in the Kintinian conglomerate below the Bidini deposit and cropping out in the Sanu Tinti deposit.

## Bracketing the timing of gold mineralisation in Siguiri

The relative timing of gold mineralisation events in the Siguiri district can be bracketed using crosscutting relationships. All gold-forming events developed in the Kintinian, Fatoya and Balato sedimentary formations, and the respective maximum age of sedimentation of these formations was dated at 2124 ± 7, 2113 ± 5 and 2113 ± 10 Ma (Lebrun et al. 2015b).

The latest gold-forming event in Siguiri is syn-$D_{4S}$, a deformation event responsible for the development of the NNE-

SSW $S_{4S}$ cleavage. This cleavage is sub-parallel to the supra-solidus magmatic fabric observed in the Malea monzogranite, which crops out to the north of the district (Fig. 1) and which was emplaced along with the Saraya volcanic breccia at 2089 ± 12 and 2092 ± 5 Ma, respectively (Lebrun et al. 2015b). Based on the orientation of the $S_{4S}$ cleavage parallel to the supra-solidus magmatic fabric in the Malea monzogranite, we interpret the emplacement of this intrusive and of the Saraya volcanic breccia to be coeval with the formation of the $S_{4S}$ cleavage recognised in the Siguiri district. The timing of the gold mineralisation events in the Siguiri district is therefore bracketed by the minimum deposition age of the Balato Formation and the crystallisation age of the Saraya volcanic breccia, between ca. 2103 Ma and ca. 2087 Ma respectively.

## Comparison with other West African orogenic gold deposits

The Siguiri mineralisation footprint has many similarities with other West African orogenic gold deposits. In particular, mineralisation at the Massawa deposit in Eastern Senegal (Treloar et al. 2015; Fig. 15) is structurally controlled and hosted along sub-vertical NE-trending shear zones similar to the Kosise deposit. Mineralisation consists of disseminated arsenopyrite and pyrite similar to that found in the Bidini-Sanu Tinti conglomerate and is associated with carbonate-sericite alteration. This first mineralisation event in Massawa is overprinted by late Au-Sb-Te veining absent in Siguiri. This overprint is associated with coarse visible gold. Mineralisation at the Sadiola Hill deposit in Western Mali (Masurel et al. 2015a; Fig. 15) is structurally controlled and hosted along sub-vertical N-S- and NNE-trending shear zones. Au-As-Sb mineralisation is mainly associated with disseminated sulphides but can also be found associated with sulphide veinlets and quartz-carbonate-sulphide-(biotite-tourmaline) veins. Potassic alteration dominates at the Sadiola Hill deposit and is associated with carbonate alteration. Mineralisation at the Yalea deposit in Western Mali (Lawrence et al. 2013a; Fig. 15) is structurally controlled and hosted along sub-vertical N-S- and NNE-trending shear zones. Mineralisation comprises quartz-ankerite-sulphide veins, similar to the Kosise style of mineralisation, and is also associated with chlorite-carbonate-sericite-quartz-albite alteration. The timing of gold mineralisation at Massawa, Sadiola Hill and Yalea can be constrained in between the maximum age of crystallisation of the South Faleme pluton and Boboti granodiorite, 2082 ± 1 and 2080 ± 1 Ma (Hirdes and Davis 2002), and the

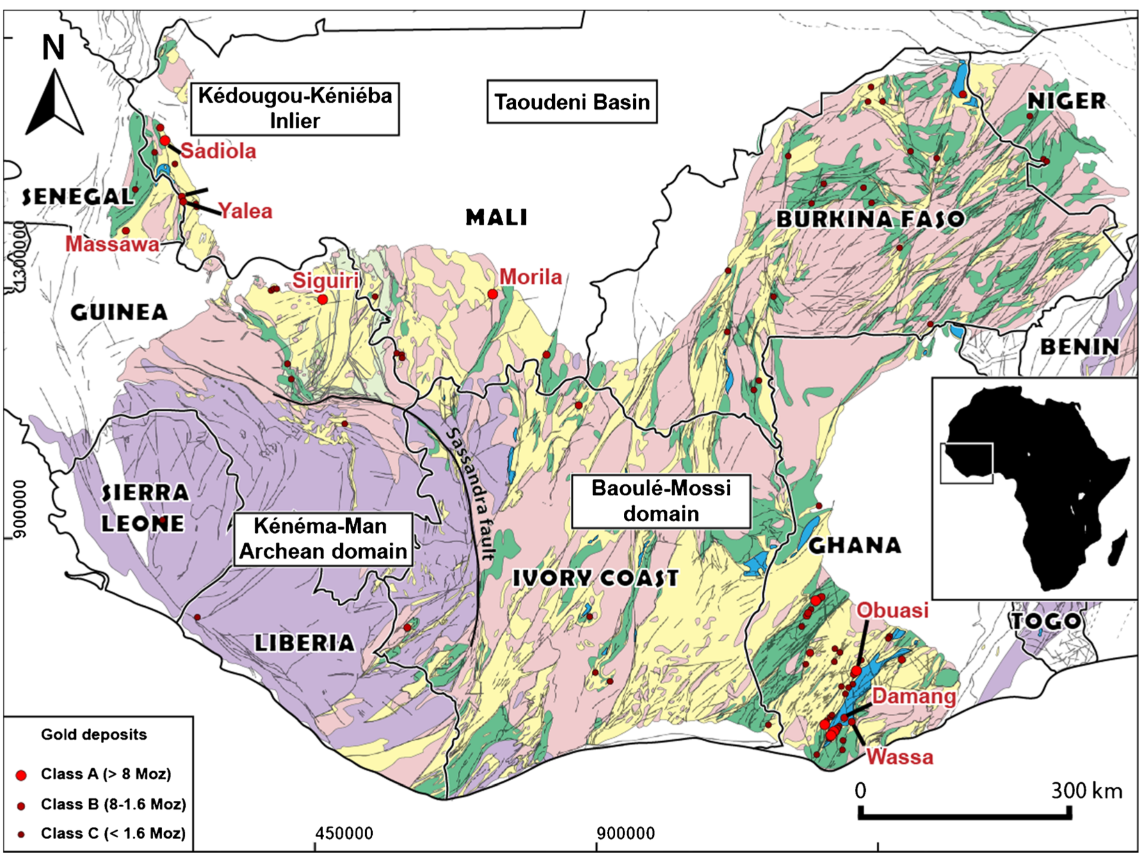


**Fig. 15** Regional geological map of the West African Craton and locations of some major gold deposits. Legend as in Fig. 1 and *light blue colour* represents Tarkwa Group sedimentary rocks. Modified after Lebrun et al. (2015b)

Saraya granite (2079 ± 2 Ma; Lawrence et al. 2013a). The South Faleme pluton and Boboti granodiorite were interpreted to be coeval with the development of iron skarns, overprinted by regional orogenic gold mineralisation in the Kédougou-Kénieba Inlier (Masurel et al. 2015b). The Saraya granite emplacement was coeval with gold mineralisation at Loulo (Lawrence et al. 2013a), a deposit presenting similar mineral alteration and gold timing to the Sadiola Hill deposit (Masurel et al. 2015b). The minimum age of gold mineralisation in Loulo is constrained by the age of crosscutting dolerite dated at 2072 ± 7 Ma (Lawrence et al. 2013a). Gold mineralisation for these deposits is therefore bracketed in between ca. 2083 and ca. 2077 Ma.

Early Au-Sb-Bi-(Te-W) mineralisation at the Morila deposit in Southeast Mali (McFarlane et al. 2011; Fig. 15) is categorised as intrusion-related but is overprinted by As-Au-Ag orogenic style mineralisation. This late overprint is hosted along a NNE-trending shear zone. Mineralisation is characterised by disseminated arsenopyrite containing polygonal gold blebs and is associated with albitisation and the development of titanite. The timing of the intrusion-related mineralisation at Morila is bracketed between the crystallisation age of the intrusives that host gold, dated at 2098 ± 4 and 2091 ± 4 Ma (McFarlane et al. 2011). The overprinting orogenic gold mineralisation, associated with datable titanite, was dated at 2074 ± 14 Ma by the same authors.

Mineralisation in the Obuasi gold mine in Ghana (Fougerouse et al. 2015; Fig. 15) is similar to that in the Siguiri district. Mineralisation in Obuasi is structurally controlled and displays two distinct textures: disseminated gold-bearing sulphides (predominantly arsenopyrite in shale) and quartz-carbonate veins associated with native gold. Obuasi mineralisation is also associated with chlorite-quartz and carbonate alteration (e.g. ankerite, siderite grains; Fougerouse et al. 2015). Other examples of a similar mineralisation

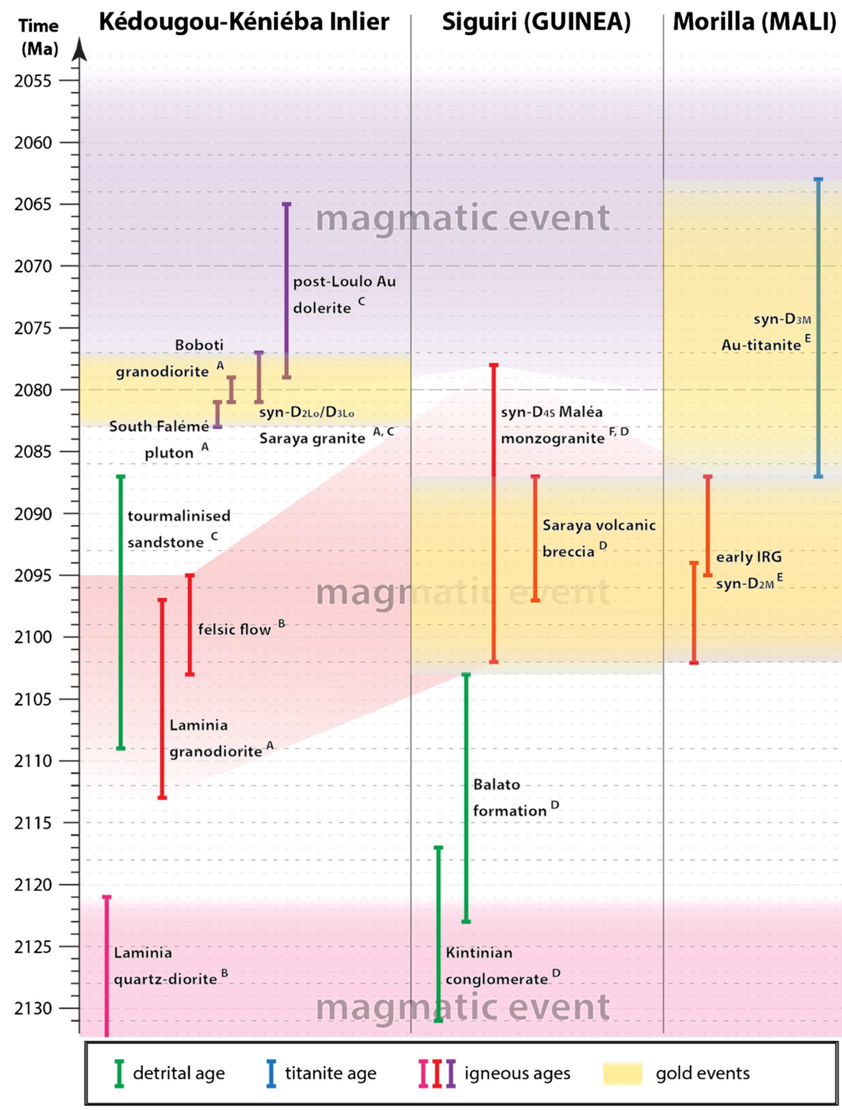


**Fig. 16** Synthetic time chart comparison of some key late Eburnean gold mineralisation events and their timing. From *A*: Dia et al. (1997), *B*: Hirdes and Davis (2002), *C*: Lawrence et al. (2013a) and Lawrence et al. (2013b), *D*: Lebrun et al. (2015a) and Lebrun et al. (2015b), *E*: McFarlane et al. (2011) and *F*: Parra-Avila (2015) and Parra-Avila et al. (2015)

footprint in West Africa include Wassa, Benso and Damang (Pigois et al. 2003; Parra-Avila et al. 2015; Fig. 15).

Based on the structural framework and geochronology of the KKI, Guinea, Mali, Ghana and other West African references (Milési et al. 1989; Milési et al. 1992), gold mineralisation in West Africa between ca. 2110 and 2060 Ma can be split into two main events (Fig. 16). Both gold mineralisation events are chronologically associated with two distinct suites of intrusive rocks previously distinguished by Hirdes and Davis (2002).

The first gold mineralisation event occurred between ca. 2102 and 2085 Ma and was coeval with a first episode of magmatism characterised by the emplacement of granodiorite and felsic flows in the KKI and quartz-diorite in the Morila deposit (McFarlane et al. 2011; Parra-Avila 2015; Fig. 16). This first magmatic event was interpreted as associated with the syn-$D_{3Lo}$ gold-tourmaline event in Loulo (KKI) and with the syn-$D_{2M}$ intrusion-related gold mineralisation in Morila and early gold mineralisation at Obuasi (Lawrence et al. 2013a; Lawrence et al. 2013b; McFarlane et al. 2011; Fougerouse et al. 2015; Fig. 15).

The second gold mineralisation event was coeval with a younger episode of magmatism responsible for the emplacement of the Saraya granite, Falémé calc-alkaline pluton, Boboti granodiorite and Loulo dolerite in the KKI (Hirdes and Davis 2002; Lawrence et al. 2013a; Masurel et al. 2015a; Fig. 16). This younger episode of magmatism, dated between ca. 2085 and 2054 Ma, is coeval with the second episode of gold mineralisation, recognised in the deposits of Loulo in the KKI, Morila in Mali, as well as Damang and Obuasi in Ghana (Hirdes and Davis 2002; McFarlane et al. 2011; Fougerouse et al. 2015; Fig. 15).

In comparison, the Siguiri district syn-$D_{3S}$ orogenic gold mineralisation ($V_{3A}$ and $V_{3B}$ veining) was overprinted by a later phase of gold mineralisation or remobilisation, syn-$D_{4S}$, coeval with the emplacement of the Malea monzogranite and Saraya volcanic breccia, which coincides with the first episode of magmatism discussed above (Fig. 16). Thus, it is proposed that the gold events in Siguiri (syn-$D_{3S}$ and syn-$D_{4S}$) occurred during the ca. 2102–2085 Ma episode of gold mineralisation recognised across the West African Craton. These conclusions have a direct impact on orogenic gold exploration as they suggest that younger economic gold mineralisation coeval with the second episode of magmatism at ca. 2085–2054 Ma, such as the late gold overprint in Morila, has yet to be discovered in the Siguiri Basin.

## Conclusion

The Siguiri district, hosted by the weakly metamorphosed sediments of the Siguiri Basin (Guinea), is characterised by a polyphase hydrothermal history and two textures (or style of mineralisation) of the hydrothermal mineral assemblages. The dominant texture, or Kosise style of mineralisation, displays vein haloes structurally controlled by early-$D_{3S}$ N-S, NE-SW, WNW-ESE and E-W fracture zones. In comparison, the other texture, or Sanu Tinti style, is only found in the conglomerate interbeds of the Kintinian Formation. The hydrothermal mineral assemblage associated with this style is disseminated and dominated by pyrite. A discreet structural control on gold mineralisation and alteration development can be observed along a N-S thrust fault marking the contact with the Fatoya Formation.

Both styles are associated with gold. The first episode of gold mineralisation is related to the development of the Kosise style $V_{3A}$ pyrite-ankerite veins in which gold can be found locked in the pyrite crystal lattice (Au values up to 43.3 ppm). The second episode of gold mineralisation is associated with the Kosise style $V_{3B}$ quartz-ankerite-arsenopyrite conjugate veins and with the Sanu Tinti style syn-$V_{3B}$ disseminated pyrite. Native gold can be found in the $V_{3B}$ veins and invisible gold (up to 55.5 ppm) can be found locked in the arsenopyrite crystal lattice. Both these gold episodes were overprinted by a late penetrative NNE-SSW $S_{4S}$ cleavage associated with minor free gold, chalcopyrite and galena infilling $V_{3A}$ pyrite and $V_{3B}$ pyrite and arsenopyrite fractures.

Geochemistry conducted in different deposits and a composite geochemical cross section across ore shoots reveals that gold mineralisation in the Siguiri district is associated with enrichments in Ag, Au, As, Bi, (Sb), Te and W, typical of mesozonal to hypozonal orogenic gold deposits. These enrichments are also accompanied by additional increases in Co, Mo, Na/Al (molar) and S and decreases in Ca, 3K/Al (molar), Mg, P, Rb and V across the main ore shoot. These chemical changes can be linked to the paragenetic sequence, are indicative of an albite-carbonate-sulphide-sericite alteration associated with the ore shoots and may increase the size of the targets for exploration.

Comparison of the syn-$D_{3S}$ and syn-$D_{4S}$ gold mineralisation timing at the Siguiri district with other orogenic gold deposits from West Africa indicates that these gold mineralisation events are coeval with other gold events recognised across the craton at ca. 2102–2085 Ma. The overprinting gold mineralisation event recognised craton-wide at ca. 2085–2054 Ma is not represented in the Siguiri district, whereas it represents the main source of gold in other deposits of the West African Craton (e.g. Morila, Loulo, Sadiola). This study supports the concept that gold mineralisation in Siguiri and in West Africa is polyphase and that careful consideration of the Siguiri district mineralisation timing could lead to future discovery of gold deposits.

**Acknowledgments** We thank the anonymous reviewers of this paper, associate editor Hartwig Frimmel and editor in chief Georges Beaudoin for their insightful recommendations and help. This project was funded by AngloGold Ashanti Limited. Eddie Connell, Shawn Kitt, Katharina Wulff and Craig Duvel are acknowledged for providing site access, support and inspiring discussions. Dr. Robert Hart is also thanked for the explanations on how to process XRD data. The authors also acknowledge the facilities and the scientific and technical assistance of the Australian Microscopy & Microanalysis Research Facility at the Centre for Microscopy, Characterisation & Analysis, the John de Laeter Centre for Isotope Research, The University of Western Australia and Curtin University.

## References

Allibone AH, McCuaig TC, Harris D, Etheridge M, Munroe S, Byrne D, Amanor J, Gyapong W (2002) Structural controls on gold mineralization at the Ashanti gold deposit, Obuasi, Ghana. Society of Economic Geologists Special publication 9:65–93

Bateman R, Hagemann S (2004) Gold mineralisation throughout about 45 Ma of Archaean orogenesis: protracted flux of gold in the Golden Mile, Yilgarn craton, Western Australia. Mineral Deposita 39:536–559

Béziat D, Naré G, Matuszak M, Le Mignot E, Salvi S, Fougerouse D, Siebenaller L, André-Mayer AS, Naba S, Franceschi G (2013 confidential) Etude pétrologique des roches magmatiques associées aux mineralisations Cu-Au du prospect de Gongondy, District de Gaoua, Burkina Faso. AMIRA International Ltd P934A - West African Exploration Initiative - Stage 2 Final report E1:446–536.

Bierlein FP, Maher S (2001) Orogenic disseminated gold in phanerozoic fold belts—examples from Victoria, Australia and elsewhere. Ore Geol Rev 18:113–148

Boiron M-C, Cathelineau M, Banks DA, Fourcade S, Vallance J (2003) Mixing of metamorphic and surficial fluids during the uplift of the Hercynian upper crust: consequences for gold deposition. Chem Geol 194:119–141

Christie AB, Brathwaite RL (2003) Hydrothermal alteration in metasedimentary rock-hosted orogenic gold deposits, Reefton goldfield, South Island, New Zealand. Mineral Deposita 38:87–107

Cook NJ, Ciobanu CL, Meria D, Silcock D, Wade B (2013) Arsenopyrite-pyrite association in an orogenic gold ore: tracing mineralization history from textures and trace elements. Econ Geol 108:1273–1283

Davis D, Hirdes W, Schaltegger U, Nunoo E (1994) U-Pb age constraints on deposition and provenance of Birimian and gold-bearing Tarkwaian sediments in Ghana, West Africa. Precambrian Res 67:89–107

Dia A, Van Schmus W, Kröner A (1997) Isotopic constraints on the age and formation of a Palaeoproterozoic volcanic arc complex in the Kedougou Inlier, eastern Senegal, West Africa. J Afr Earth Sci 24:197–213

Dubé B, Gosselin P (2007) Greenstone-hosted quartz-carbonate vein deposits. Mineral deposits of Canada: a synthesis of major deposit-types, district metallogeny, the evolution of geological provinces, and exploration methods: Geological Association of Canada, Mineral Deposits Division, Special Publication 5:49–73.

Eilu P, Groves D (2001) Primary alteration and geochemical dispersion haloes of Archaean orogenic gold deposits in the Yilgarn Craton: the pre-weathering scenario. Geochem Explor Environ Anal 1:183–200

Eilu P, Mikucki EJ (1998) Alteration and primary geochemical dispersion associated with the Bulletin lode-gold deposit, Wiluna, Western Australia. J Geochem Explor 63:73–103

Eilu PS, Mathison CI, Groves DI, Allardyce WJ (1999) Atlas of alteration assemblages, styles and zoning in orogenic lode-gold deposits in a variety of host rock and metamorphic settings. Geology and Geophysics Department (Centre for Strategic Mineral Deposits) & UWA Extension, The University of Western Australia, Publication 30.

Fougerouse D, Micklethwaite S, Halfpenny A, Kilburn M, Ulrich S (2015) Gold remobilisation from Arsenopyrite: crystal-plasticity and dissolution-reprecipitation reactions. Proceeding of the 13th Biennial SGA Meeting 2015, Mineral Resources in a Sustainable World, 4:1611–1614

Fougerouse D, Micklethwaite S, Ulrich S, Miller J, Godel B, Adams DT, McCuaig TC (2016) Evidence for two stages of mineralization in West Africa's largest gold deposit: Obuasi, Ghana. Econ Geol (in press)

Goldfarb RJ, Baker T, Dube B, Groves DI, Hart CJ, Gosselin P (2005) Distribution, character, and genesis of gold deposits in metamorphic terranes. Economic Geology 100th Anniversary Volume:407–450.

Grant JA (2005) Isocon analysis: a brief review of the method and applications. Phys Chem Earth 30:997–1004

Gresens RL (1967) Composition-volume relationships of metasomatism. Chem Geol 2:47–65

Groves D (1993) The crustal continuum model for late-Archaean lode-gold deposits of the Yilgarn Block, Western Australia. Mineral Deposita 28:366–374

Groves DI, Goldfarb RJ, Gebre-Mariam M, Hagemann S, Robert F (1998) Orogenic gold deposits: a proposed classification in the context of their crustal distribution and relationship to other gold deposit types. Ore Geol Rev 13:7–27

Groves DI, Goldfarb RJ, Knox-Robinson CM, Ojala J, Gardoll S, Yun GY, Holyland P (2000) Late-kinematic timing of orogenic gold deposits and significance for computer-based exploration techniques with emphasis on the Yilgarn Block, Western Australia. Ore Geol Rev 17:1–38

Groves DI, Goldfarb RJ, Robert F, Hart CJ (2003) Gold deposits in metamorphic belts: overview of current understanding, outstanding problems, future research, and exploration significance. Econ Geol 98:1–29

Heinrich CA (2007) Fluid-fluid interactions in magmatic-hydrothermal ore formation. Rev Mineral Geochem 65:363–387

Hirdes W, Davis D (2002) U–Pb geochronology of paleoproterozoic rocks in the southern part of the Kedougou-Kenieba Inlier, Senegal, West Africa: evidence for diachronous accretionary development of the Eburnean province. Precambrian Res 118:83–99

Hirdes W, Nunoo B (1994) The Proterozoic paleoplacers at Tarkwa gold mine, SW Ghana; sedimentology, mineralogy, and precise age dating of the Main Reef and West Reef, and bearing of the investigations on source area aspects. Geologisches Jahrbuch D 100:247–311

Ho S, Groves D, McNaughton N, Mikucki E (1992) The source of ore fluids and solutes in Archaean lode-gold deposits of Western Australia. J Volcanol Geotherm Res 50:173–196

Kishida A, Kerrich R (1987) Hydrothermal alteration zoning and gold concentration at the Kerr-Addison Archean lode gold deposit, Kirkland Lake, Ontario. Econ Geol 82:649–690

Landry B (1995) Prospection minière. Modulo, Mont-Royal, Québec

Large RR, Bull SW, Maslennikov VV (2011) A carbonaceous sedimentary source-rock model for Carlin-type and orogenic gold deposits. Econ Geol 106:331–358

Large R, Thomas H, Craw D, Henne A, Henderson S (2012) Diagenetic pyrite as a source for metals in orogenic gold deposits, Otago Schist, New Zealand. New Zeal J Geol Geophys 55:137–149

Lawrence DM, Treloar PJ, Rankin AH, Boyce A, Harbidge P (2013b) A fluid inclusion and stable isotope study at the Loulo mining district, Mali, West Africa: implications for multifluid sources in the generation of orogenic gold deposits. Econ Geol 108:229–257

Lawrence DM, Treloar PJ, Rankin AH, Harbidge P, Holliday J (2013a) The geology and mineralogy of the Loulo Mining District, Mali, West Africa: evidence for two distinct styles of orogenic gold mineralization. Econ Geol 108:199–227

Lebrun E, Thébaud N, Miller J, Ulrich S, Bourget J, Terblanche O (2015b) Geochronology and lithostratigraphy of the Siguiri district: implications for gold mineralisation in the Siguiri Basin (Guinea, West Africa). Precambrian Res 274:136–160

Lebrun E, Ulrich S, Miller J, Thébaud N, McCuaig C (2015a) The world-class Siguiri gold district, Siguiri Basin, Guinea (West Africa): stress switches within an orogenic gold system. Econ Geol.

López-Moro FJ (2012) EASYGRESGRANT—A Microsoft Excel spreadsheet to quantify volume changes and to perform mass-balance modeling in metasomatic systems. Comput Geosci 39: 191–196

MacLean W, Barrett T (1993) Lithogeochemical techniques using immobile elements. J Geochem Explor 48:109–133

Masurel Q, Thébaud N, Miller J, Ulrich S, Hein KAA (2015b) The Alamoutala carbonate-hosted gold deposit in Mali, West Africa. Ore Geol Rev. doi: 10.1016/j.oregeorev.2015.10.012.

Masurel Q, Thébaud N, Miller J, Ulrich S, Hein K, Cameron G, Béziat D, Bruguier O, Davis J (2015a) Sadiola Hill: a world-class carbonate-hosted gold deposit in Mali, West Africa. Econ Geol.

McFarlane CRM, Mavrogenes J, Lentz D, King K, Allibone A, Holcombe R (2011) Geology and intrusion-related affinity of the Morila gold mine, Southeast Mali. Econ Geol 106:727–750

Milési JP, Feybesse JL, Ledru P, Dommanget A, Ouedraogo MF, Marcoux E, Prost A, Vinchon C, Sylvain JP, Johan V, Teguey M, Calvez JY, Lagny P (1989) Les minéralisations aurifères de l'Afrique de l'Ouest. Leurs relations avec l'evolution lithostructurale au Protérozoïque inférieur Chronique de la recherche minière 497:3–98

Milési J-P, Ledru P, Feybesse J-L, Dommanget A, Marcoux E (1992) Early Proterozoic ore deposits and tectonics of the Birimian orogenic belt, West Africa. Precambrian Res 58:305–344

Miller JM, Davis J, Baratoux L, McCuaig TC, Metelka V, Jessel M (2013) Evolution of gold systems in Guinea, southern Mali and western Burkina Faso. AMIRA International Ltd P934A - West African Exploration Initiative - Stage 2 Unpubl. Final report D1: 127–234

Mukherjee P, Gupta P (2008) Arbitrary scaling in ISOCON method of geochemical mass balance: an evaluation of the graphical approach. Geochem J 42:247–253

Neumayr P, Walshe J, Hagemann S, Petersen K, Roache A, Frikken P, Horn L, Halley S (2008) Oxidized and reduced mineral assemblages in greenstone belt rocks of the St. Ives gold camp, Western Australia: vectors to high-grade ore bodies in Archaean gold deposits? Mineral Deposita 43:363–371

Oberthür T, Vetter U, Davis DW, Amanor JA (1998) Age constraints on gold mineralization and Paleoproterozoic crustal evolution in the Ashanti belt of southern Ghana. Precambrian Res 89:129–143

Parra-Avila LA (2015) 4D Evolution of the Paleoproterozoic Baoulé-Mossi Domain of the West African Craton: PhD thesis. Centre for Exploration Targeting, University of Western Australia, 527 p.

Parra-Avila LA, Bourassa Y, Miller J, Perrouty S, Fiorentini ML, McCuaig TC (2015) Age constraints of the Wassa and Benso Mesothermal gold deposits, Ashanti Belt, Ghana, West Africa. J Afr Earth Sci 112:524–535

Passchier CW, Trouw RAJ (2005) MICROTECTONICS. Springer. 366 p.

Pigois J-P, Groves DI, Fletcher IR, McNaughton NJ, Snee LW (2003) Age constraints on Tarkwaian palaeoplacer and lode-gold formation in the Tarkwa-Damang district, SW Ghana. Mineral Deposita 38: 695–714

Pitcairn IK, Teagle DA, Craw D, Olivo GR, Kerrich R, Brewer TS (2006) Sources of metals and fluids in orogenic gold deposits: insights from the Otago and Alpine Schists, New Zealand. Econ Geol 101:1525–1546

Price RE, Pichler T (2006) Abundance and mineralogical association of arsenic in the Suwannee limestone (Florida): implications for arsenic release during water–rock interaction. Chem Geol 228:44–56

Ramsay JG, Huber MI (1987) The techniques of modern structural geology: vol.2: folds and fractures. Academic Press, London, 392 p.

Reich M, Kesler SE, Utsunomiya S, Palenik CS, Chryssoulis SL, Ewing RC (2005) Solubility of gold in arsenian pyrite. Geochim Cosmochim Acta 69:2781–2796

Ridley JR, Diamond LW (2000) Fluid chemistry of orogenic lode gold deposits and implications for genetic models. SEG Reviews 13:141–162

Robert F, Poulsen KH, Cassidy KF, Hodgson CJ (2005) Gold metallogeny of the Superior and Yilgarn cratons. Econ Geol 100: 1001–1033

Salier BP, Groves DI, McNaughton NJ, Fletcher IR (2005) Geochronological and stable isotope evidence for widespread orogenic gold mineralization from a deep-seated fluid source at ca 2.65 Ga in the Laverton gold province, Western Australia. Econ Geol 100:1363–1388

Savage KS, Tingle TN, O'Day PA, Waychunas GA, Bird DK (2000) Arsenic speciation in pyrite and secondary weathering phases, Mother Lode gold district, Tuolumne County, California. Appl Geochem 15:1219–1244

Sinclair A (1974) Selection of threshold values in geochemical data using probability graphs. J Geochem Explor 3:129–149

Sinclair A (1991) A fundamental approach to threshold estimation in exploration geochemistry: probability plots revisited. J Geochem Explor 41:1–22

Taylor R (2010) Ore textures: recognition and interpretation. Springer Science & Business Media.

Tomkins AG (2013) On the source of orogenic gold. Geology 41:1255–1256

Treloar PJ, Lawrence DM, Senghor D, Boyce A, Harbidge P (2015) The Massawa gold deposit, Eastern Senegal, West Africa: an orogenic gold deposit sourced from magmatically derived fluids? Geol Soc Lond, Spec Publ 393(1):135–160

Voicu G, Bardoux M, Stevenson R, Jebrak M (2000) Nd and Sr isotope study of hydrothermal scheelite and host rocks at Omai, Guiana Shield: implications for ore fluid source and flow path during the formation of orogenic gold deposits. Mineral Deposita 35:302–314

Wilkinson J, Boyce A, Earls G, Fallick A (1999) Gold remobilization by low-temperature brines; evidence from the Curraghinalt gold deposit, Northern Ireland. Econ Geol 94:289–296

Zhao H-X, Frimmel HE, Jiang S-Y, Dai B-Z (2011) LA-ICP-MS trace element analysis of pyrite from the Xiaoqinling gold district, China: implications for ore genesis. Ore Geol Rev 43:142–153